REPORT DOCUMENTATION PAGE

Form Approved
OMB NO. 0704-0188

1. AGENCY USE ONLY (Leave Blank)	2. REPORT DATE	3. REPORT TYPE AND DATES COVERED
	26 March 2003	Final Report (7/9/01-12/31/02)

4. TITLE AND SUBTITLE
ADVANCED COMPOSITE PERFORMANCE: MATERIAL BEHAVIOR AND LIFE CYCLE PREDICTION FOR ROTATING MACHINES

5. FUNDING NUMBERS
DAAD19-01-1-0694

6. AUTHOR(S)
Scott W. Case and Kenneth L. Reifsnider

7. PERFORMING ORGANIZATION NAME(S) AND ADDRESS(ES)
Virginia Polytechnic Institute and State University
120 Patton Hall Mail Code 0219
Blacksburg VA 24061

8. PERFORMING ORGANIZATION REPORT NUMBER

9. SPONSORING / MONITORING AGENCY NAME(S) AND ADDRESS(ES)
U. S. Army Research Office
P.O. Box 12211
Research Triangle Park, NC 27709-2211

10. SPONSORING / MONITORING AGENCY REPORT NUMBER
42451-EG
. 1

11. SUPPLEMENTARY NOTES
The views, opinions and/or findings contained in this report are those of the author(s) and should not be construed as an official Department of the Army position, policy or decision, unless so designated by other documentation.

12 a. DISTRIBUTION / AVAILABILITY STATEMENT
Approved for public release; distribution unlimited.

12 b. DISTRIBUTION CODE

13. ABSTRACT (Maximum 200 words)

The Virginia Tech life prediction methodology is applied to composite materials to determine a fundamental understanding of material behavior and life cycle issues (e.g. fatigue damage, creep, creep rupture). Specific areas addressed in this activity include: (1) establishing the likely damage and failure modes for rotating machines; (2) constructing micromechanical models of the material failure modes; (3) constructing a methodology for the life analysis of composite rotors operating under high temperature and loading.

14. SUBJECT TERMS
composite materials, lifetime prediction, creep rupture, fatigue

15. NUMBER OF PAGES
60

16. PRICE CODE

17. SECURITY CLASSIFICATION OR REPORT	18. SECURITY CLASSIFICATION ON THIS PAGE	19. SECURITY CLASSIFICATION OF ABSTRACT	20. LIMITATION OF ABSTRACT
UNCLASSIFIED	UNCLASSIFIED	UNCLASSIFIED	UL

REPORT DOCUMENTATION PAGE (SF298)
(Continuation Sheet)

ADVANCED COMPOSITE PERFORMANCE: MATERIAL BEHAVIOR AND LIFE CYCLE PREDICTION FOR ROTATING MACHINES

TABLE OF CONTENTS

Problem Under Consideration

The Virginia Tech life prediction methodology is applied to composite materials to determine a fundamental understanding of material behavior and life cycle issues (e.g. fatigue damage, creep, creep rupture). Specific areas addressed to date in this activity include: (1) establishing the likely damage and failure modes for rotating machines; (2) constructing micromechanical models of the material failure modes; (3) constructing a methodology for the life analysis of composite rotors operating under high temperature and loading.

Key Results

In this effort, model predictions have been compared to the experimental strength distribution of a carbon fiber/polymer matrix composite. Initially, the only material variability included in the prediction is the fiber strength distribution. For this case, the computed strength distribution is much narrower than experimentally observed. Including additional sources of material variability such as distributed fiber volume fractions, initial fiber fractures, and non-uniform fiber placement in the modeling yield results that are in excellent agreement with the experimental strength distribution. It is shown that of all the additional sources of material variability considered, distributed fiber volume fractions have the greatest effect on the computed strength.

Additionally, micromechanical models with no adjustable material parameters have been developed for the stress rupture lifetime of unidirectional polymer composites loaded in the fiber direction. A general time-dependent load-sharing framework is developed by applying shear-lag assumptions. The time-dependent load-sharing methodologies are included into Monte Carlo simulations to compute stress rupture lifetime. The simulation approach is best suited to address the critical question of material reliability for a desired lifetime under a given set of external conditions. Comparisons are made to the rupture lifetime of a carbon fiber/polymer matrix composite. We have found encouraging quantitative agreement between the model composite measurements and the time-dependent load-sharing results. In addition, we have found (based upon the modeling results) that one of the common assumptions made in predicting composite lifetimes (the strength-life equal rank assumption) is invalid for stress rupture lifetime prediction. Our simulation results also explain the large variations in measured composite rupture lifetimes. In particular, it has been shown that a narrower fiber strength distribution results in longer lifetimes with greater variability. Also, changing a certain combination of input parameters that controls the perturbed length of fiber due to a break does not produce any change in computed rupture lifetime. Since the load-sharing is time and temperature dependent, lifetime predictions can be made at different temperatures. Hence, the method presented here can be used to help understand and predict the role of temperature in accelerated measurement of stress rupture lifetimes. The results of this effort have been incorporated into a journal article that is in review by the *International Journal of Solids and Structures* [1]. We have also been able to incorporate the results from these micromechanical models of stress rupture lifetime into residual strength based lifetime predictions (the *MRLife* approach) to predict combined fatigue and stress rupture effects.

To validate these predictions, we have been involved in a collaborative effort with the Center for Electromechanics at the University of Texas at Austin. Two different types of specimen geometry have been considered: "flat coupons" fabricated by filament winding of T1000G/977-2 around a nominally flat panel and rings also fabricated by filament winding. The flat coupons were to be used for initial validation of the modeling. The tests considered were quasi-static tension, tension-tension fatigue loading (R=0.1), and stress rupture at two temperatures. The results of the tensile testing are summarized in Table I. As expected, we see considerable reduction in the tensile strength as a function of testing temperature (at 200ºF and 275ºF).

Table I. Quasi-static test results

Temperature (°F)	Modulus (msi)	Strength (ksi)	Failure Strain (%)	# tests
70	25.3 ± 0.26	409 ± 35	-	5
200	22.6 ± 1.0	339 ± 22	1.497 ± 0.198	5
275	23.7 ± 0.46	364 ± 34	1.476 ± 0.076	5

The results of the fatigue tests are shown in Figure 1. There is a considerable reduction in fatigue lifetime at 275ºF, although there are some concerns as a large percentage of the failures occurred in the vicinity of the grip region.

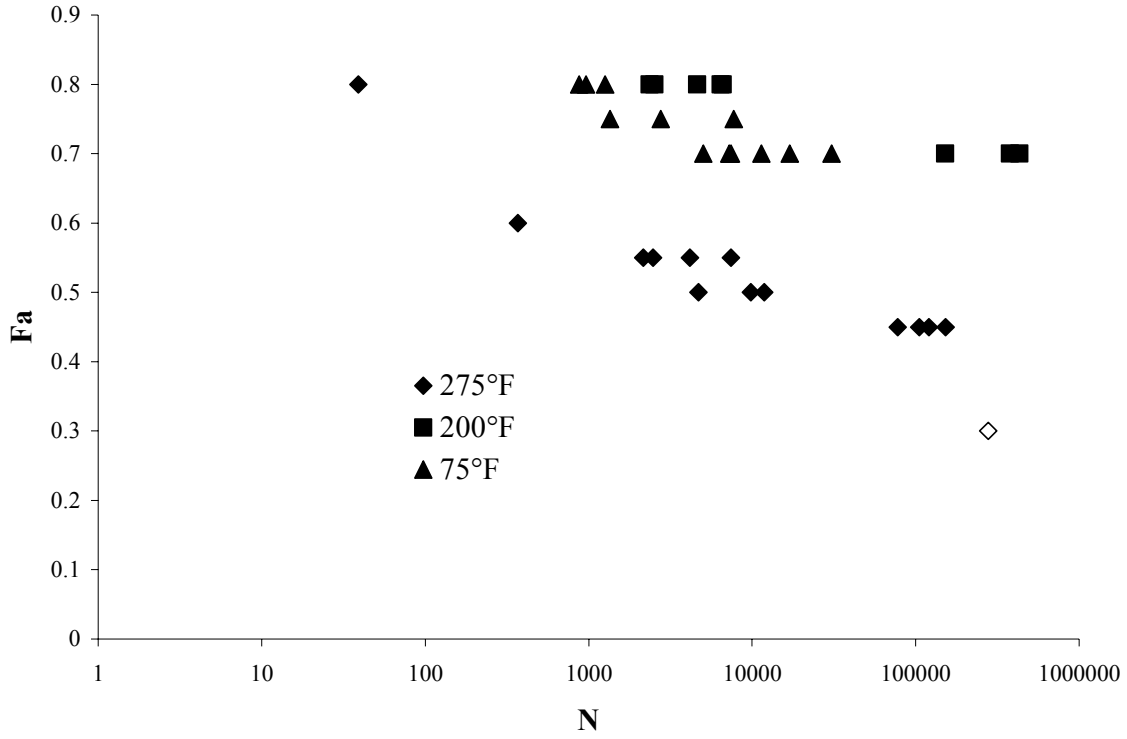

Figure 1. Tension-tension fatigue test results on T1000G/977-2 coupons. The value of Fa (the failure criterion) corresponds to the maximum fatigue stress divided by the ultimate strength at the corresponding temperature.

A total of 4 stress-rupture tests were run at 200°F. All either survived 25 hours of stress or slipped. Two runouts were at Fa = 0.8 and a third was at 0.7. All had remaining strengths higher than the initially measured quasi-static strength. The final test was an incremental stress test designed to obtain creep data for the composite. Several stress levels were examined using the same specimen and the stress-time profile is shown in Figure 2. The resultant strain is shown in Figure 3. The measured creep rates were on the order of 10^{-9}/sec.

At 275°F, 7 tests were run. A number of other tests failed during the initial ramp. The results are shown in Figure 4. Two tests failed after approximately 10 hours, while the remaining five survived at least 25 hours. For these tests, the remaining strength was approximately 90% of the initial strength.

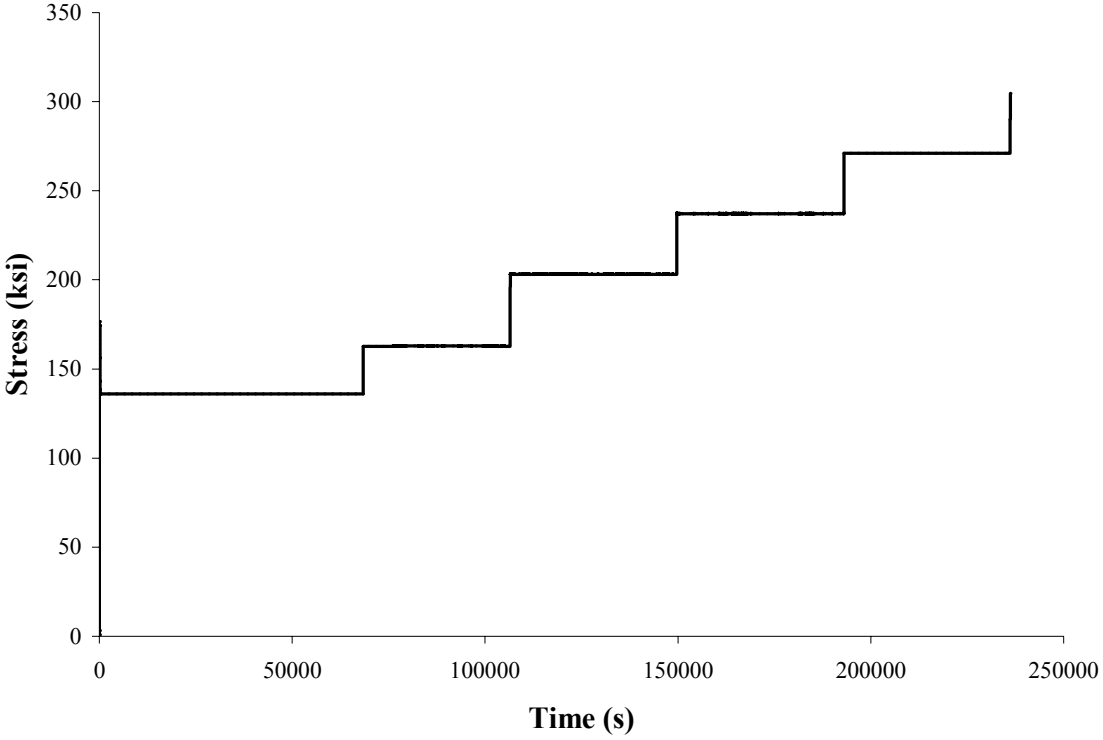

Figure 2. Stress-time profile

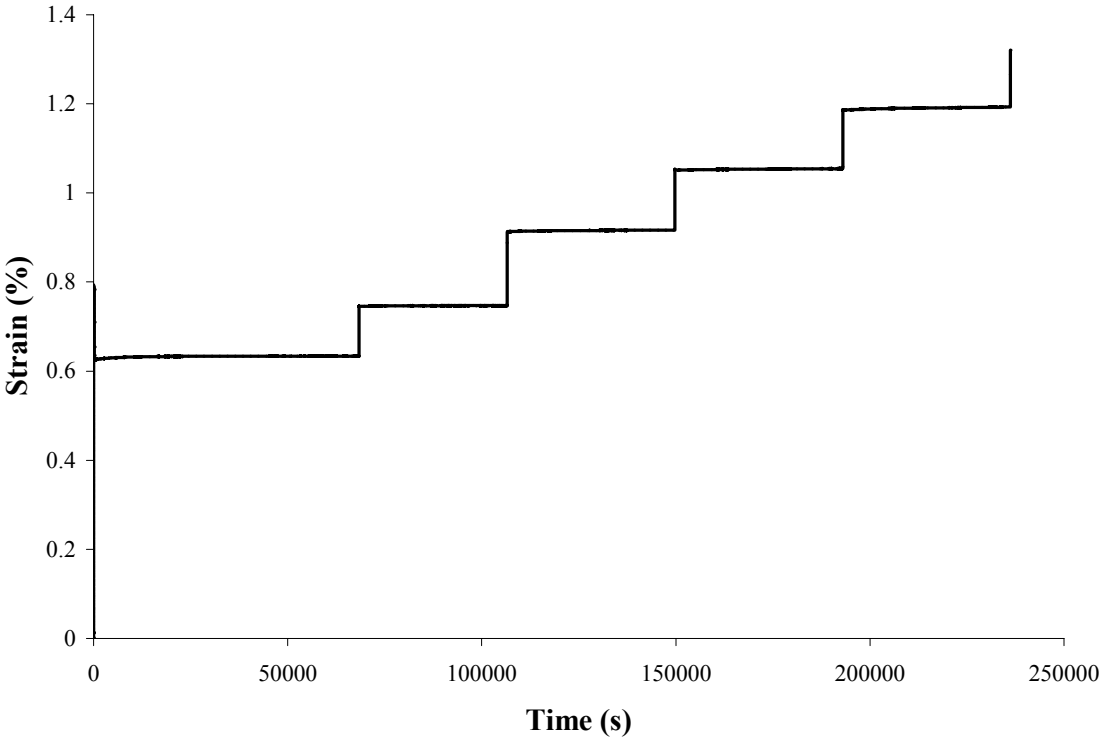

Figure 3. Strain versus time for incremental load test

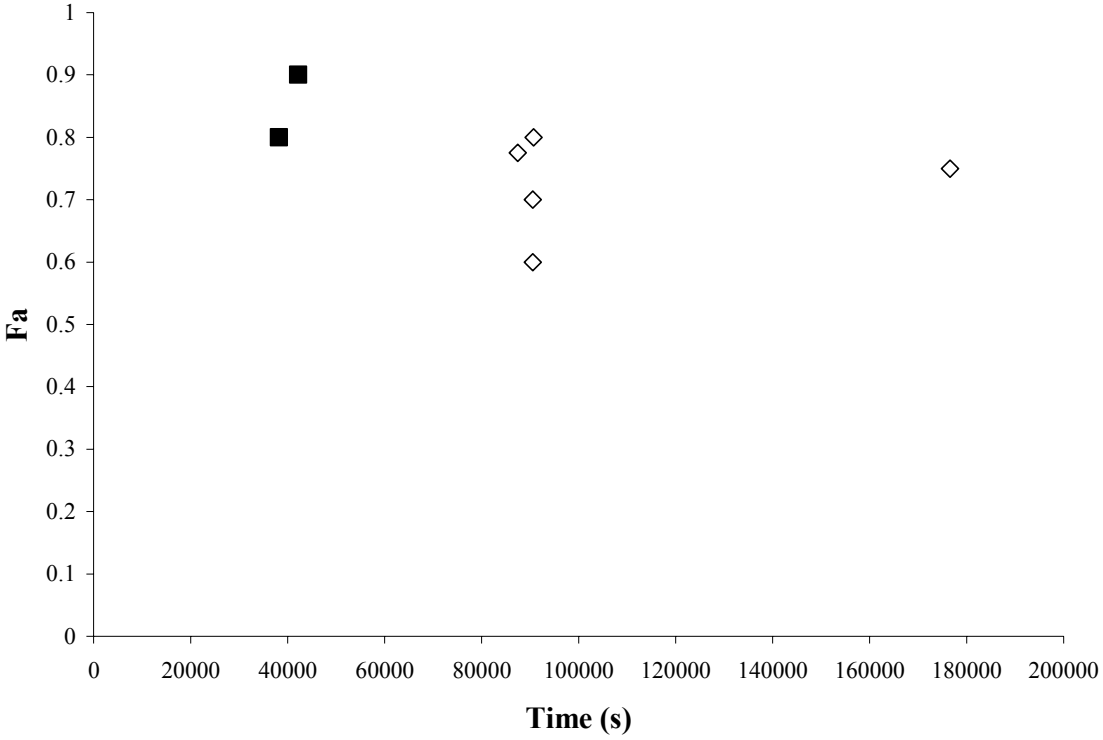

Figure 4. 275°F stress-rupture results

In addition to these coupon tests, hydroburst tests were conducted on the ring samples. To date, three burst tests have been run successfully. Two were room temperature quasi-static burst and the third was a 200°F quasi-static burst test. A stress-rupture test at 200°F was abandoned due to failure of the seal. At 75°F the burst pressures were 3005 psi and 3191 psi. These corresponded to hoop stresses of 470.9 ksi and 497.6 ksi. At 200°F the burst pressure was 3127 psi corresponding to a hoop stress of 486.8 ksi. The measured modulus at 75°F was 31 msi and has not been measured at 200°F. These strengths are much higher than the corresponding values for the coupons, suggesting that grip failures may have occurred (perhaps due to the initial curvature of these nominally flat coupons).

Publications and Presentations

The following publications have resulted from this work:

Journal Article: Bandorawalla, T., Russell, B., Davison, S., and Case, S. "Micromechanics-Based Lifetime Prediction of Polymer Composites," submitted to *International Journal of Solids and Structures*, April 2002.

Conference Proceedings Article: Krasnikovs, A., Bandorawalla, T., and Case, S. "The Effect of Viscoelastic local relaxation at fibre breaks on time dependent failure in unidirectional materials," **Keynote Address** to be presented at Durability Analysis of Composite Systems: DURACOSYS 2003, San Diego, July 20-23, 2003.

Presentation: Case, S., Lesko, J. and Reifsnider, K., "Strength-Based Lifetime Prediction of Composite Materials," Invited Lecture for DARPA Durability Workshop, Woodland Hills, CA, December 5-6, 2001.

Scientific Personnel

The first graduate student on this project (Tozer Bandorawalla) was awarded second place in the Virginia Tech College of Engineering Paul E. Torgersen Graduate Student Research Excellence Award. This competitive award recognizes outstanding research efforts by College of Engineering graduate students. He is currently employed by Intel.

The second graduate student on this project (Sneha Patel Davison) has been awarded a P.E.O. scholar award, and will complete her Ph.D. studies in July 2003.

The PI on this project (Scott Case) was named the Virginia Tech College of Engineering's Outstanding New Assistant Professor Award for 2002 based on his teaching and research achievements.

The project has also been used to partially support a post-doctoral research assistant (Dr. Howard Halverson) who is responsible for experimental characterization of the composite materials, as well as model development.

Inventions

There were no inventions associated with this project.

Technology Transfer

This work was conducted in collaboration with Richard Thompson at the University of Texas-Center for Electromechanics (CEM) (funded by the Army separately). Data generated at CEM was used for validation of the models developed in this study, and the analysis codes developed at Virginia Tech are being transferred to CEM to aid in its design process, thus providing a leveraging of the Army investment.

To facilitate transfer to the Army, the results of the analysis techniques developed in this study have been incorporated into the *MRLife* lifetime prediction of composites code. This is a Microsoft Windows compatible program with documentation to provide a stand-alone lifetime prediction analysis for composites subjected to mechanical and environmental loading conditions.

Bibliography

[1] T. Bandorawalla, B. E. Russell, S. R. Patel, and S. W. Case, "Micromechanics-Based Life Prediction of Polymer Composites," submitted to *International Journal of Solids and Structures*.

APPENDIX

MICROMECHANICS-BASED LIFE PREDICTION OF POLYMER COMPOSITES

T. BANDORAWALLA,[*] B. E. RUSSELL,[†] S. R. PATEL,[‡] S. W. CASE[§]
Department of Engineering Science & Mechanics
Virginia Polytechnic Institute and State University, Blacksburg, VA 24061, U.S.A.

Abstract – This paper develops a Monte Carlo simulation technique to predict the stress-rupture lifetime of longitudinally loaded unidirectional polymer composites based on fiber and matrix properties. Matrix viscoelasticity is cited as the primary cause of rupture failure. Time-dependent matrix deformation leads to an increase in the overstressed length of unbroken fibers in the vicinity of a cluster of fiber fractures. A general time-dependent load-sharing framework that is able to account for an arbitrary sequence of fiber fractures is developed. Matrix deformations are based on the shear-lag assumption. The time-dependent load sharing is incorporated into a Monte Carlo simulation for stress-rupture lifetime. Even though the only material variability included in the simulation is the fiber strength distribution, very broad lifetime distributions are computed. The reasons for broad rupture lifetime distributions are discussed. It is shown that the strength-life equal rank assumption does not apply for unidirectional polymer composites loaded in longitudinal tension because of fundamental differences between quasi-static and stress-rupture failure behavior. Encouraging comparisons are made to the experimental rupture lifetime of carbon fiber/polymer matrix composites. Finally, recommendations for improving the testing procedures for stress rupture of unidirectional composite materials are made.

Keywords – Creep, Static fatigue, Reliability, Probability, Fiber stress redistribution

1 INTRODUCTION

The use of composite materials in engineering applications requires an understanding of their behavior under various loading conditions. In particular, as composite materials are deployed in applications where several years of reliable service life are required, predictions of long-term

[*] Corresponding author. Present address: Fax: E-mail:

[†] Visteon Corp. Rawsonville Plant, McKean & Textile Rd.,Ypsilanti, MI 48197, U.S.A.

[‡] 219 Norris Hall, Virginia Polytechnic Institute and State University, Blacksburg, VA 24061, U.S.A.

[§] 120 Patton Hall, Virginia Polytechnic Institute and State University, Blacksburg, VA 24061, U.S.A.

durability are necessary. Because of the myriad of possible combinations of fiber and matrix materials, the best-case situation would be to make such predictions in terms of constituent properties. This is the goal of the present study for the case in which failure is governed by tensile failure of the fibers in the composite. A key aspect of this work is use of Monte Carlo simulations for lifetime prediction. There is ample experimental evidence that the rupture lifetime of a material is not deterministic. Hence, it is extremely important for life-prediction techniques to be able to determine component reliability at a given stress level for a desired lifetime. The models presented in this work utilize probabilistic techniques to account for variability in fiber strength that translate into variability in lifetime.

An important aspect of this work is time-dependent fiber stress redistribution, or load-sharing, in the vicinity of broken fibers. Hedgepeth (1961) and Hedgepeth and Van Dyke (1967) introduced influence-function techniques to model quasi-static load sharing. In this work time-dependent models for load sharing are required by assuming linearly elastic properties for the fibers and linearly viscoelastic matrix properties. Lagoudas *et. al.* (1989) and Beyerlein *et. al.* (1998) have developed time-dependent load-sharing models within the shear-lag framework. Lagoudas *et. al.* developed exact, closed-form, and approximate load-sharing solutions for a single unidirectional composite lamina with a cluster of adjacent coplanar fiber fractures. They also extended their results to consider a growing cluster of coplanar breaks. Beyerlein *et. al.* developed a more general approach called viscous break interaction (VBI). They presented approximate and numerical techniques for arbitrarily positioned fiber fractures occurring simultaneously in a three-dimensional volume of material. Although Beyerlein *et. al.* did suggest alterations to consider breaks that occurred sequentially in time, they did not present a complete analysis. Moreover, both Lagoudas *et. al.* and Beyerlein *et. al.* assumed a power law creep compliance model for the matrix material. In this work we present a general approximate numerical framework for time-dependent load sharing that is able to account for arbitrarily positioned fiber fractures that occur sequentially in time. A direct Laplace inversion approximation introduced by Schapery (1967) is used for the analysis. This approximation makes it possible to accommodate a more general creep law that can be expressed as a Prony series. Section 2 discusses two different shear-lag based load-sharing methods: the traditional approach of Hedgepeth and Van Dyke, and a simplification where the load of a broken fiber is redistributed

only onto its nearest neighbors. The two methods are compared to each other in Section 3. A qualitative comparison is also made to time-dependent strain concentration measurements on model composites (Bandorawalla *et. al.*, 2002a).

Lifshitz and Rotem (1970) were the first to develop a micromechanical theory for stress-rupture of composite materials consisting of brittle fibers with probabilistic strengths embedded in a viscoelastic matrix. It was widely believed that stress-rupture of polymer composites resulted from the time-dependent strength of some fibers (e.g. glass fibers). Lifshitz and Rotem used their model to show that delayed failure can occur even when the fiber strengths are not time-dependent. Since most of the literature dealt with stress-rupture of glass-reinforced materials, Lifshitz (1971) conducted some preliminary tests to show that the stress-rupture phenomenon occurred in carbon-reinforced epoxies even though carbon fibers are widely believed to be free of any creep response. Section 3 presents further experimental and theoretical confirmation of the mechanism that leads to delayed failure of longitudinally loaded unidirectional polymer composites even when fiber strengths are not time-dependent.

In this work we develop Monte Carlo simulations to model the stress-rupture process in composites with a viscoelastic matrix. Ibnabdeljalil and Phoenix (1995) have used similar Monte Carlo simulations to investigate the statistics of composite failure in brittle matrix composites resulting from fiber strength degradation. Along similar lines, Iyengar and Curtin (1997a and 1997b) implemented Monte Carlo simulations for stress-rupture of metal and ceramic matrix composites due to the combined effect of strength degradation of the fibers, and matrix and interfacial shear creep. Iyengar and Curtin (1997b) used the formulation of Du and McMeeking (1995) to model the effect of matrix creep resulting from time-dependent relaxation of normal and shear stresses in metal and ceramic matrix composites. Theoretical models have also been developed to predict stress-rupture lifetimes of simple model composite systems with few fibers (Phoenix *et. al.*, 1988; Otani *et. al.*, 1991). Making comparisons of the model predictions with rupture lifetimes of carefully controlled model systems provides valuable insight into the rupture failure process that helps with modeling “real” composite systems.

Section 4 develops the general stress-rupture simulation framework for longitudinally loaded unidirectional polymer composites consisting of linearly elastic fibers with Weibull strengths and a linearly elastic matrix. Unidirectional polymer composites consistently fail in or near the gripped section of the specimen. In order to alleviate this problem stress-rupture lifetimes are measured on an AS-4 carbon fiber/polyetheretherketone (PEEK) laminate with $[90/0_3]_s$ layup. The 90° surface plies carry a negligible fraction of the total load on the material and protect the inner core of load-carrying 0° plies. Quasi-static strengths and rupture lifetime measurements on the AS-4/PEEK composite system are presented. Comparisons between the rupture predictions and measurements on the AS-4/PEEK system are also presented in Section 4. Section 5 discusses the reasons for large variability in lifetime predictions by performing a study of the effect of certain material parameters on lifetime. Section 5 also discusses the fundamental reasons why the strength-life equal rank assumption is not valid for modeling stress-rupture of unidirectional polymer composites. The models further reinforce why it is necessary to prevent any initial grip-induced damage while measuring the rupture lifetime of unidirectional polymer composites. Finally in Section 6, the major results and conclusions are summarized.

2 TIME-DEPENDENT LOAD SHARING

Bandorawalla *et. al.* (2002b) introduced a quasi-static framework to calculate the micromechanical fiber stress redistribution due to arbitrary fiber facture locations. The technique was based in superposition of the effect of individual fiber fractures. In this paper a similar framework is required that is able to compute time-dependent fiber stresses due to an arbitrary sequence of fiber fractures. The time-dependent version is considerably more complicated. The times at which fiber fractures occurred and their locations need to be taken into account to calculate the fiber stresses at any position and time. This general time-dependent framework for load-sharing is developed in Section 2.1. The fibers are assumed to be linearly elastic, while the matrix is assumed to be linearly viscoelastic. It is shown that the effect of each fiber fracture is expressed as a convolution of the crack tip opening-displacement at the fiber fracture location and a time-dependent force influence-function. The force influence-functions depend on geometric and material properties of the composite, and assumptions of the mechanism of load transfer (i.e. shear-lag, finite element) and number of neighboring fibers involved in this transfer. Once again we draw on experience with modeling quasi-static load

sharing to compute the force influence-functions. Two different types of load sharing are developed in Sections 2.2 and 2.3 depending on the technique used to calculate the force influence-functions. They are called Nearest Neighbor Load Sharing (NNLS) and Hedgepeth and Van Dyke Load Sharing (HVDLS). NNLS was developed by Bandorawalla *et. al.* (2002b) to model quasi-static fiber stress redistribution in unidirectional polymer composites. NNLS assumes that the load of a broken fiber is redistributed only onto the nearest neighbors. The authors believe that NNLS may be valid for time-dependent stress redistribution too. HVDLS is a time-dependent extension of the traditional quasi-static technique introduced by Hedgepeth and Van Dyke (1967). In HVDLS the load of a broken fiber is transferred onto all the surrounding fibers with preferential load transfer to the nearer fibers. A comparison between the time-dependent stresses calculated by the two approaches is made in Section 3.

2.1 *General Time-Dependent Load Sharing Concepts*

Consider a regular array of $N \times M$ hexagonally packed fibers of length X, as shown in Figure 1. The x-coordinate system is oriented perpendicular to the cross-sectional plane of the fibers. This is the volume of material that will be considered for the Monte Carlo simulations for stress rupture presented in Section 4. A far-field tensile axial stress $\sigma_{ff}\,\mathrm{H}(t)$, is applied to the fibers, where $\mathrm{H}(t)$ is the Heaviside unit step function.

The purpose of this section is to present a framework for calculation of axial fiber stress $\sigma_{n,m}(x,t)$, in fiber (n, m), at time t, due an arbitrary sequence of fiber fractures occurring prior to time t. Let $b_1, b_2, b_3 \ldots b_r$ fiber fractures occur at times $t_1, t_2, t_3 \ldots t_r$, respectively, such that $0 \le t_1 < t_2 < t_3 \ldots t_r \le t$. The total number of fiber fractures that have occurred by t_i is $L_i = b_1 + \ldots + b_i$ for $i = 1,2,\ldots r$. Hence, a total number of L_r fiber fractures have occurred by time t. For convenience the fiber fractures are sequentially numbered as $1, 2,\ldots L_r$. The fractures $1, 2,\ldots L_r$ occur in fibers $(n_1, m_1), (n_2, m_2)\ldots(n_{Lr}, m_{Lr})$ at axial locations $x_1, x_2 \ldots x_{Lr}$, respectively. At t_i the fiber fractures designated $L_{i-1}+1$ through L_i occur. Naturally, $L_0 = 0$. Due to the far-field tensile stress σ_{ff}, the broken fiber ends are separated by a displacement $2u_{n_i,m_i}(x_i,t)$, $i = 1,2,\ldots L_r$. The quantities $u_{n_i,m_i}(x_i,t)$, $i = 1,2,\ldots L_r$ will be referred to as break opening-displacements. $\sigma_{n,m}^{t_k}(x,t)$, $k =$

1,2,…r, represent the fiber stresses at $t \geq t_r$ due to only the L_k fiber fractures that have occurred by t_k. Similarly, $u^{t_k}_{n_i,m_i}(x_i,t)$, k = 1,2,…r, represent the break opening-displacements at $t \geq t_r$ due to only the L_k fiber fractures that have occurred by t_k. The only non-zero $u^{t_k}_{n_i,m_i}(x_i,t)$ are for i = 1,2,…L_k. Hence, the fiber stresses and break opening-displacements at t are given by

$$\sigma_{n,m}(x,t) = \sigma^{t_r}_{n,m}(x,t) \tag{1}$$

and

$$u_{n_i,m_i}(x_i,t) = u^{t_r}_{n_i,m_i}(x_i,t) \tag{2}$$

respectively. $\sigma^{t_r}_{n,m}(x,t)$ and $u^{t_r}_{n_i,m_i}(x_i,t)$ are calculated from the recursive relations

$$\sigma^{t_k}_{n,m}(x,t) = \sigma^{t_{k-1}}_{n,m}(x,t) + \sigma^{k}_{n,m}(x,t-t_k)\,\mathrm{H}(t-t_k) \tag{3}$$

and

$$u^{t_k}_{n_i,m_i}(x_i,t) = u^{t_{k-1}}_{n_i,m_i}(x_i,t) + u^{k}_{n_i,m_i}(x_i,t-t_k)\,\mathrm{H}(t-t_k) \tag{4}$$

$\sigma^{k}_{n,m}(x,t-t_k)$, k = 1…r represents the change in fiber stresses produced due to the set of b_k fractures that occur at t_k. Similarly, $u^{k}_{n_i,m_i}(x_i,t-t_k)$, k = 1…r represents the change in break opening displacements produced by the set of b_k fractures that occur at t_k. Once again, the only non-zero $u^{k}_{n_i,m_i}(x_i,t-t_k)$ are for i = 1…L_k. If $\sigma^{k}_{n,m}(x,t-t_k)$ and $u^{k}_{n_i,m_i}(x_i,t-t_k)$ are known the fiber stresses and break opening-displacements are readily obtained from Equations (1) through (4). It should be pointed out that the virgin material state has no fiber fractures. Hence when applying Equation (3) and (4) with k = 1, break opening-displacements $u^{t_0}_{n_i,m_i}(x_i,t)$ are non-existent and $\sigma^{t_0}_{n,m}(x,t)$ = σ_{ff} H(t). The remainder of Section 2.1 outlines the approach to calculate $\sigma^{k}_{n,m}(x,t-t_k)$ and $u^{k}_{n_i,m_i}(x_i,t-t_k)$. It is convenient to calculate $u^{k}_{n_i,m_i}(x_i,t-t_k)$ and $\sigma^{k}_{n,m}(x,t-t_k)$ in Laplace domain since the governing system of equations involve convolution integrals that are converted into a system of linear algebraic equations by Laplace transformation. The time-domain results are then obtained in an approximate sense by Schapery's (1967) direct Laplace inversion given by

$$\mathrm{f}(t) \approx \left\langle s\,\overline{\mathrm{F}}(s)\right\rangle\Big|_{s=1/2t} \tag{5}$$

where $\overline{\mathrm{F}}(s)$ is the Laplace transform of f(t) i.e. $\mathcal{L}$ [f(t)] = $\overline{\mathrm{F}}(s)$.

Representative curves for $\sigma^{t_k}_{n_i,m_i}(x_i,t)$ and $u^{t_k}_{n_i,m_i}(x_i,t)$ as given by Equation (3) and (4), respectively, are shown in Figure 2 through Figure 7. The fiber stresses at $t \geq t_r$ due to only the L_k fiber fractures that have occurred by t_k are given by

$$\sigma^{t_k}_{n,m}(x,t) = \sigma_{ff}\,\mathrm{H}(t) + \sum_{j=1}^{L_k}\int_0^t \mathrm{Q}_{n-n_j,m-m_j}\left(x-x_j,t-\beta\right)\frac{\partial u^{t_k}_{n_j,m_j}\left(x_j,\beta\right)}{\partial\beta}\mathrm{d}\beta \tag{6}$$

Equation (6) is simply an expression of superposition of the far-field stress and the perturbation due to each fiber break in the composite material. $\mathrm{Q}_{n,m}(x,t)$ is the axial stress produced in fiber (n, m), at location x, calculated by applying a Heaviside unit step opening-displacement, i.e. H(t), to a break in fiber (0,0) at x = 0. $\mathrm{Q}_{n,m}(x,t)$ is called the time-dependent force influence-function. $\mathrm{Q}_{n,m}(x,t)$ depends on geometric and constitutive properties of the fibers and matrix and the load sharing assumptions i.e. NNLS, HVDLS, shear-lag, etc. Calculation of $\mathrm{Q}_{n,m}(x,t)$ is presented in Section 2.2 and 2.3.

To begin the solution process, we note that the Laplace transform of Equation (6) is given by

$$\overline{\sigma}^{t_k}_{n,m}(x,s) = \frac{\sigma_{ff}}{s} + \sum_{j=1}^{L_k}\overline{\mathrm{Q}}_{n-n_j,m-m_j}\left(x-x_j,s\right)s\,\overline{u}^{t_k}_{n_j,m_j}\left(x_j,s\right) \tag{7}$$

From Figure 2 through Figure 4 it is apparent that Equation (4) can be simplified to

$$u^{t_k}_{n_i,m_i}(x_i,t) = u^{k}_{n_i,m_i}(x_i,t-t_k)\mathrm{H}(t-t_k)\text{, for } i = L_{k\text{-}1}{+}1\ldots L_k \tag{8}$$

since these fiber fractures $i = L_{k\text{-}1}{+}1\ldots L_k$ do not exist until t_k. Comparing Equation (8) with Equation (4) reiterates that

$$u^{t_{k-1}}_{n_i,m_i}(x_i,t) = 0\text{, for } i = L_{k\text{-}1}{+}1\ldots L_k \tag{9}$$

i.e. breaks $i = L_{k-1}+1 \ldots L_k$ do not exist before t_k. Equation (4) applies as is for all breaks $i = 1 \ldots L_{k-1}$ (i.e. the breaks that exist before t_k). Substituting the Laplace transforms of Equations (4) and (8) into Equation (7) yields

$$\begin{aligned}\overline{\sigma}_{n,m}^{t_k}(x,s) = \frac{\sigma_{ff}}{s} + \sum_{j=1}^{L_{k-1}} \overline{\mathrm{Q}}_{n-n_j,m-m_j}(x-x_j,s)\, s\left[\overline{u}_{n_j,m_j}^{t_{k-1}}(x_j,s) + \overline{u}_{n_j,m_j}^{k}(x_j,s)\, e^{-st_k}\right] + \\ \sum_{j=L_{k-1}+1}^{L_k} \overline{\mathrm{Q}}_{n-n_j,m-m_j}(x-x_j,s)\, s\, \overline{u}_{n_j,m_j}^{k}(x_j,s) e^{-st_k}\end{aligned} \tag{10}$$

We can rewrite Equation (7) to find $\overline{\sigma}_{n,m}^{t_{k-1}}(x,s)$

$$\overline{\sigma}_{n,m}^{t_{k-1}}(x,s) = \frac{\sigma_{ff}}{s} + \sum_{j=1}^{L_{k-1}} \overline{\mathrm{Q}}_{n-n_j,m-m_j}(x-x_j,s)\, s\, \overline{u}_{n_j,m_j}^{t_{k-1}}(x_j,s) \tag{11}$$

Substituting Equation (11) into Equation (10) yields

$$\overline{\sigma}_{n,m}^{t_k}(x,s) = \overline{\sigma}_{n,m}^{t_{k-1}}(x,s) + \sum_{j=1}^{L_k} \overline{\mathrm{Q}}_{n-n_j,m-m_j}(x-x_j,s)\, s\, \overline{u}_{n_j,m_j}^{k}(x_j,s) e^{-st_k} \tag{12}$$

Comparing the Laplace transform of Equation (3) with Equation (12) shows that

$$\overline{\sigma}_{n,m}^{k}(x,s) = \sum_{j=1}^{L_k} \overline{\mathrm{Q}}_{n-n_j,m-m_j}(x-x_j,s)\, s\, \overline{u}_{n_j,m_j}^{k}(x_j,s) \tag{13}$$

Applying Equation (12) to the break locations $1 \ldots L_k$ yields a system of equations given by

$$\begin{aligned}\overline{\sigma}_{n_i,m_i}^{t_k}(x_i,s) = \overline{\sigma}_{n_i,m_i}^{t_{k-1}}(x_i,s) \\ + \sum_{j=1}^{L_k} \overline{\mathrm{Q}}_{n_i-n_j,m_i-m_j}(x_i-x_j,s)\, s\, \overline{u}_{n_j,m_j}^{k}(x_j,s) e^{-st_k}, \text{ for } i = 1,2,\ldots L_k\end{aligned} \tag{14}$$

In order to calculate the unknowns $\overline{u}_{n_j,m_j}^{k}(x_j,s)$, j=1,2,…L_k, in Equation (14) it is necessary to consider two separate cases. For Case I, Equation (14) is applied to the location of breaks that occurred before t_k. For Case II, Equation (14) is applied to the location of breaks that occur at t_k.

2.1.1 Case I ($i = 1 \ldots L_{k-1}$)

From Figure 5 through Figure 7 it is apparent that Equation (3) can be simplified to

$$\sigma_{n_i,m_i}^{t_k}(x_i,t) = \sigma_{n_i,m_i}^{t_{k-1}}(x_i,t), \text{ for } i = 1 \ldots L_{k-1} \tag{15}$$

since these fiber fractures have occurred by $t_{k\text{-}1}$. The state of stress at (n_i, m_i) and x_i, $i = 1\ldots L_{k\text{-}1}$ is unchanged by any further fiber fractures that occur after $t_{k\text{-}1}$. This is reinforced by comparing Equation (15) with Equation (3) which implies that

$$\sigma^{k}_{n_i,m_i}\left(x_i, t-t_k\right)\mathrm{H}\left(t-t_k\right)=0\text{, for } i=1\ldots L_{k\text{-}1} \tag{16}$$

Substituting the Laplace transform of Equation (15) into Equation (14) yields the system of equations given by

$$0=\sum_{j=1}^{L_k}\overline{\mathrm{Q}}_{n_i-n_j,m_i-m_j}\left(x_i-x_j,s\right)s\,\overline{u}^{k}_{n_j,m_j}\left(x_j,s\right)\text{, for } i=1\ldots L_{k\text{-}1} \tag{17}$$

Equation (17) requires that the additional break opening-displacements that occur at t_k do not alter the stress state at the location of breaks that occurred before t_k.

2.1.2 Case II ($i = L_{k\text{-}1}+1\ldots L_k$)

Applying Equation (3) to the stress at breaks $i = L_{k\text{-}1}+1\ldots L_k$ yields

$$\sigma^{t_k}_{n_i,m_i}\left(x_i,t\right)=\sigma^{t_{k-1}}_{n_i,m_i}\left(x_i,t\right)+\sigma^{k}_{n_i,m_i}\left(x_i,t-t_k\right)\mathrm{H}\left(t-t_k\right) \tag{18}$$

From Figure 5 through Figure 7 it is apparent that

$$\sigma^{k}_{n_i,m_i}\left(x_i,t-t_k\right)\mathrm{H}\left(t-t_k\right)=-\sigma^{t_{k-1}}_{n_i,m_i}\left(x_i,t\right)\mathrm{H}\left(t-t_k\right)\text{, for } i=L_{k\text{-}1}+1\ldots L_k \tag{19}$$

since the stresses at (n_i, m_i) and x_i, $i = L_{k\text{-}1}+1\ldots L_k$ go to zero at t_k. Substituting the Laplace transform of Equation (18) into Equation (14) yields the system of equations given by

$$\overline{\sigma}^{k}_{n_i,m_i}\left(x_i,s\right)=\sum_{j=1}^{L_k}\overline{\mathrm{Q}}_{n_i-n_j,m_i-m_j}\left(x_i-x_j,s\right)s\,\overline{u}^{k}_{n_j,m_j}\left(x_j,s\right)\text{, for } i=L_{k\text{-}1}+1\ldots L_k \tag{20}$$

Equation (20) together with Equation (19) requires that the additional break opening-displacements at t_k cause the stresses at the location of breaks that occur at t_k to vanish.

Collectively, Equations (17) and (20) represent L_k linear algebraic equations that can be solved for $\overline{u}^{k}_{n_j,m_j}\left(x_j,s\right)$, $j = 1\ldots L_k$, provided $\overline{\sigma}^{k}_{n_i,m_i}\left(x_i,s\right)$ in Equation (20) is known. It will be shown that Equation (19) can be used to obtain $\overline{\sigma}^{k}_{n_i,m_i}\left(x_i,s\right)$, $i = L_{k\text{-}1}+1\ldots L_k$. Once $\overline{u}^{k}_{n_j,m_j}\left(x_j,s\right)$, $j = 1\ldots L_k$ are calculated, the Laplace transform of Equation (4) and (2) can be used to calculate the

break opening-displacements in Laplace domain. Moreover, Equation (13), and the Laplace transforms of Equations (3) and (1) can be used to calculate the fiber stresses in Laplace domain. Hence, a complete solution to the problem is readily available in Laplace domain. In order to calculate the time-domain solution Equation (5) is used as described below.

Within the context of Schapery's direct inversion

$$\mathcal{L}^{-1}\left\{ \mathrm{e}^{-sa}\ \overline{\mathrm{F}}(s) \right\} \approx \mathrm{H}(t-a) \left\langle s\, \overline{\mathrm{F}}(s) \right\rangle \Big|_{s=1/2(t-a)} \tag{21}$$

Hence, the approximate inverse Laplace transform of Equation (12) is

$$\sigma_{n,m}^{t_k}(x,t) \approx \sigma_{n,m}^{t_{k-1}}(x,t) + \sum_{j=1}^{L_k} \mathrm{H}(t-t_k) \left\langle \overline{\mathrm{Q}}_{n-n_j,m-m_j}(x-x_j,s)\, s^2\ \overline{u}_{n_j,m_j}^{k}(x_j,s) \right\rangle \Big|_{s=\frac{1}{2(t-t_k)}} \tag{22}$$

Similarly, Equation (4) becomes

$$u_{n_i,m_i}^{t_k}(x_i,t) \approx u_{n_i,m_i}^{t_{k-1}}(x_i,t) + \mathrm{H}(t-t_k) \left\langle s\ \overline{u}_{n_i,m_i}^{k}(x_i,s) \right\rangle \Big|_{s=\frac{1}{2(t-t_k)}} \tag{23}$$

From Equations (22) and (23) it is apparent that $\overline{u}_{n_j,m_j}^{k}(x_j,s)$, $j = 1 \ldots L_k$, is required at $s = 1/[2(t-t_k)]$. Hence, the solution to Equations (17) and (20) is obtained at $s = 1/[2(t-t_k)]$ for each $k = 1 \ldots r$. Equations (17), (20), (22), and (23) are used recursively starting with $k = 1$ through $k = r$. The final time-domain fiber stresses and break opening-displacements are given by Equations (1) and (2), respectively.

We still need to calculate $\overline{\sigma}_{n_i,m_i}^{k}(x_i,s)$, $i = L_{k-1}+1 \ldots L_k$ in Equation (20). For $t \geq t_k$ Equation (19) is simply

$$\sigma_{n_i,m_i}^{k}(x_i,t-t_k) = -\sigma_{n_i,m_i}^{t_{k-1}}(x_i,t), \text{ for } i = L_{k-1}+1 \ldots L_k \tag{24}$$

Making the change of variables $t' = t - t_k$ in Equation (24) gives

$$\sigma_{n_i,m_i}^{k}(x_i,t') = -\sigma_{n_i,m_i}^{t_{k-1}}(x_i,t'+t_k), \text{ for } i = L_{k-1}+1 \ldots L_k, \text{ and } t' \geq 0 \tag{25}$$

Within the context of Laplace inversion given by Equation (5)

$$\overline{\mathrm{F}}(s) \approx \frac{1}{s}\mathrm{f}\left(\frac{1}{2s}\right) \tag{26}$$

Using Equation (26) to evaluate the Laplace transform of $\sigma^{k}_{n_i,m_i}(x_i,t')$

$$\overline{\sigma}^{k}_{n_i,m_i}(x_i,s) \approx \frac{1}{s}\sigma^{k}_{n_i,m_i}\left(x_i,\frac{1}{2s}\right) \tag{27}$$

Using Equation (25) to evaluate the to evaluate the right hand side of Equation (27) gives

$$\overline{\sigma}^{k}_{n_i,m_i}(x_i,s) \approx -\frac{1}{s}\sigma^{t_{k-1}}_{n_i,m_i}\left(x_i,\frac{1}{2s}+t_k\right), \text{ for } i = L_{k-1}+1\ldots L_k \tag{28}$$

Hence, within the Laplace inversion approximation given by Equation (5), Equation (28) is the left hand side of Equation (20). As mentioned earlier, Equations (17) and (20) are solved for $\overline{u}^{k}_{n_j,m_j}(x_j,s), j = 1\ldots L_k$, at $s = 1/[2(t\text{-}t_k)]$. Evaluating Equation (28) at $s = 1/[2(t\text{-}t_k)]$ gives

$$\overline{\sigma}^{k}_{n_i,m_i}(x_i,s)\Big|_{s=\frac{1}{2(t-t_k)}} \approx -2(t-t_k)\,\sigma^{t_{k-1}}_{n_i,m_i}(x_i,t), \text{ for } i = L_{k-1}+1\ldots L_k \tag{29}$$

Equation (29) is substituted into Equation (20). Because of the recursive approach to solving the problem starting with $k = 1,2,\ldots r$, $\sigma^{t_{k-1}}_{n,m}(x,t)$ on the right hand side of Equation (29) is available for all (n, m) and x before $\overline{u}^{k}_{n_j,m_j}(x_j,s), j = 1\ldots L_k$, is calculated.

2.2 *Time-Dependent NNLS*

In order to implement the general load-sharing framework discussed in Section 2.1, it is necessary to obtain the Laplace transform of the force influence-functions i.e. $\overline{\mathrm{Q}}_{n,m}(x,s)$. As mentioned in Section 2.1, $\mathrm{Q}_{n,m}(x,t)$ is the axial stress produced in fiber (n, m), at location x, due to a unit step opening-displacement, i.e. H(t), at an isolated break in fiber (0,0) at $x = 0$. If uniform hexagonal packing is assumed, every fiber fracture location perturbs its surroundings in exactly the same manner. Hence, only a single set of Laplace-domain force influence-functions, with $n = 1\text{-}N\ldots N\text{-}1$, $m = 1\text{-}M\ldots M\text{-}1$, $x = -X\ldots X$, needs to be calculated.

The analysis in this section is based on NNLS assumptions. Consider a typical broken fiber (i, j), as shown in Figure 1. Fiber (i, j) has a break at $x = 0$. Under NNLS assumptions, only the axial fiber stresses within the hexagonal area are perturbed due to this single break. This would imply that all the force influence-functions expect for $Q_{0,0}(x,t)$, $Q_{1,0}(x,t)$, $Q_{0,1}(x,t)$, $Q_{-1,1}(x,t)$, $Q_{-1,0}(x,t)$, $Q_{0,-1}(x,t)$, $Q_{1,-1}(x,t)$ are identically equal to zero. Moreover, the perturbation due to a fiber fracture decreases rapidly for axial distance x, from the fiber fracture plane. For distances greater than x_p from the plane of a fiber fracture, the stress perturbation vanishes. This length x_p, is a function of the fiber and matrix stiffness and the fiber volume fraction. Also, due to symmetry all the force influence-functions of the nearest neighbors are equal i.e. $Q_{1,0}(x,t) = Q_{0,1}(x,t) = Q_{-1,1}(x,t) = Q_{-1,0}(x,t) = Q_{0,-1}(x,t) = Q_{1,-1}(x,t)$, and $Q_{n,m}(-x,t) = Q_{n,m}(x,t)$ for all (n,m). Hence for NNLS, it is only necessary to calculate $\overline{Q}_{0,0}(x,s)$ and $\overline{Q}_{1,0}(x,s)$ for $x = [0, x_p]$. Once $\overline{Q}_{0,0}(x,s)$ and $\overline{Q}_{1,0}(x,s)$ are calculated for $x = [0\ x_p]$ the foregoing load sharing is applicable for any axial length $X > x_p$.

For notational convenience in the discussion that follows, the broken fiber and its six neighbors are numbered from 1-7 as shown in Figure 1. Hence, $Q_{0,0}(x,t) = Q_1(x,t)$, $Q_{1,0}(x,t) = Q_4(x,t)$, $Q_{0,1}(x,t) = Q_3(x,t)$, etc. Let $v_1(x,t)$, $v_2(x,t)$,…$v_7(x,t)$ be the displacements of fibers 1 through 7, respectively. Under shear-lag assumptions

$$\{Q\} = E_f \frac{\mathrm{d}}{\mathrm{d}x}\{V\}$$

$$\text{where } \{Q\} = \begin{Bmatrix} Q_1(x,t) \\ Q_2(x,t) \\ Q_3(x,t) \\ Q_4(x,t) \\ Q_5(x,t) \\ Q_6(x,t) \\ Q_7(x,t) \end{Bmatrix} = \begin{Bmatrix} Q_{0,0}(x,t) \\ Q_{-1,1}(x,t) \\ Q_{0,1}(x,t) \\ Q_{1,0}(x,t) \\ Q_{1,-1}(x,t) \\ Q_{0,-1}(x,t) \\ Q_{-1,0}(x,t) \end{Bmatrix} \text{ and } \{V\} = \begin{Bmatrix} v_1(x,t) \\ v_2(x,t) \\ v_3(x,t) \\ v_4(x,t) \\ v_5(x,t) \\ v_6(x,t) \\ v_7(x,t) \end{Bmatrix} \tag{30}$$

As shown in Figure 1, the distance between the centers of two adjacent fibers is denoted by d, and $w = d - 2r_f$, where r_f is the fiber radius. Let $G_m(t)$ be the shear relaxation modulus of the matrix, E_f be the fiber axial Young's modulus, and A_f be the fiber cross-sectional area. Shear-lag

assumptions are applied to the seven highlighted fibers in Figure 1 and the governing system of equations for fiber displacements is obtained as

$$\frac{\partial^2 v_1}{\partial x^2} + C\int_0^t G_m(t-\beta)\frac{\partial}{\partial\beta}\left[v_2(x,\beta)+v_3(x,\beta)+v_4(x,\beta)+v_5(x,\beta)+v_6(x,\beta)+v_7(x,\beta)-6v_1(x,\beta)\right]d\beta = 0$$

$$\frac{\partial^2 v_2}{\partial x^2} + C\int_0^t G_m(t-\beta)\frac{\partial}{\partial\beta}\left[v_7(x,\beta)+v_1(x,\beta)+v_3(x,\beta)-3v_2(x,\beta)\right]d\beta = 0$$

$$\frac{\partial^2 v_3}{\partial x^2} + C\int_0^t G_m(t-\beta)\frac{\partial}{\partial\beta}\left[v_2(x,\beta)+v_1(x,\beta)+v_4(x,\beta)-3v_3(x,\beta)\right]d\beta = 0$$

$$\frac{\partial^2 v_4}{\partial x^2} + C\int_0^t G_m(t-\beta)\frac{\partial}{\partial\beta}\left[v_3(x,\beta)+v_1(x,\beta)+v_5(x,\beta)-3v_4(x,\beta)\right]d\beta = 0 \qquad (31)$$

$$\frac{\partial^2 v_5}{\partial x^2} + C\int_0^t G_m(t-\beta)\frac{\partial}{\partial\beta}\left[v_6(x,\beta)+v_1(x,\beta)+v_4(x,\beta)-3v_5(x,\beta)\right]d\beta = 0$$

$$\frac{\partial^2 v_6}{\partial x^2} + C\int_0^t G_m(t-\beta)\frac{\partial}{\partial\beta}\left[v_7(x,\beta)+v_1(x,\beta)+v_5(x,\beta)-3v_6(x,\beta)\right]d\beta = 0$$

$$\frac{\partial^2 v_7}{\partial x^2} + C\int_0^t G_m(t-\beta)\frac{\partial}{\partial\beta}\left[v_2(x,\beta)+v_1(x,\beta)+v_6(x,\beta)-3v_7(x,\beta)\right]d\beta = 0$$

where

$$C = \frac{h}{A_f E_f w} \qquad (32)$$

h is the thickness of the matrix shear spring that can be approximated as $h = (\pi r_f)/3$. The boundary conditions for calculating the influence-functions are

$$v_1(0,t) = \mathrm{H}(t)\ ;$$
$$v_2(0,t) = v_3(0,t) = v_4(0,t) = v_5(0,t) = v_6(0,t) = v_7(0,t) = 0 \ \text{ for t} \geq 0; \qquad (33)$$
$$\text{and } \left.\frac{\partial v_n(x,t)}{\partial x}\right|_{x=\infty} = 0\ , \text{ for } n = 1\ldots7 \text{ and t} \geq 0;$$

and the initial conditions are

$$v_n(x,0) = 0\ , \text{ for } n = 1\ldots7,\ x = [0,\ \infty] \qquad (34)$$

The Laplace transform of Equation (31) is

$$\frac{\mathrm{d}^2}{\mathrm{d}x^2}\left\{\overline{V}\right\} + s\,\overline{G}_m(s)\,C\left[A\right]\left\{\overline{V}\right\} = 0 \tag{35}$$

where

$$\text{where } \left\{\overline{V}\right\} = \begin{Bmatrix} \overline{v}_1(x,s) \\ \overline{v}_2(x,s) \\ \overline{v}_3(x,s) \\ \overline{v}_4(x,s) \\ \overline{v}_5(x,s) \\ \overline{v}_6(x,s) \\ \overline{v}_7(x,s) \end{Bmatrix}, \text{ and } \left[A\right] = \begin{bmatrix} -6 & 1 & 1 & 1 & 1 & 1 & 1 \\ 1 & -3 & 1 & 0 & 0 & 0 & 1 \\ 1 & 1 & -3 & 1 & 0 & 0 & 0 \\ 1 & 0 & 1 & -3 & 1 & 0 & 0 \\ 1 & 0 & 0 & 1 & -3 & 1 & 0 \\ 1 & 0 & 0 & 0 & 1 & -3 & 1 \\ 1 & 1 & 0 & 0 & 0 & 1 & -1 \end{bmatrix} \tag{36}$$

The Laplace transform of the boundary conditions given by Equation (33) is

$$\begin{gathered} \overline{v}_1(0,s) = 1/s; \\ \overline{v}_2(0,s) = \overline{v}_3(0,s) = \overline{v}_4(0,s) = \overline{v}_5(0,s) = \overline{v}_6(0,s) = \overline{v}_7(0,s) = 0; \\ \text{and } \left.\frac{\mathrm{d}\overline{v}_n(x,s)}{\mathrm{d}x}\right|_{x=\infty} = 0, \text{ for } n = 1\ldots7 \end{gathered} \tag{37}$$

Equations (35) through (37) represent a boundary value problem in x. The eigenvalues of $[A]$ are $-\lambda_1, -\lambda_2, \ldots -\lambda_7$, and the orthonormal eigenvectors of $[A]$ are $\{V_1\}, \{V_2\}, \ldots \{V_7\}$. Since $[A]$ is a real symmetric matrix, it is always possible to find a set of orthonormal eigenvectors. The solution of the system of Equations (35) through (37) is given by

$$\{\overline{V}\} = \left[\widetilde{V}\right] \begin{Bmatrix} \frac{a_1}{s}\exp\left[-\sqrt{s\overline{G}_m(s)C\lambda_1}\,x\right] \\ \frac{a_2}{s}\exp\left[-\sqrt{s\overline{G}_m(s)C\lambda_2}\,x\right] \\ \vdots \\ \frac{a_7}{s}\exp\left[-\sqrt{s\overline{G}_m(s)C\lambda_7}\,x\right] \end{Bmatrix}$$

where $\left[\widetilde{V}\right] = \left[\{V_1\} \quad \{V_2\} \quad \cdots \quad \{V_7\}\right]$, and

$$\begin{Bmatrix} a_1 \\ a_2 \\ a_3 \\ a_4 \\ a_5 \\ a_6 \\ a_7 \end{Bmatrix} = \left[\widetilde{V}\right]^{\mathrm{T}} \begin{Bmatrix} 1/s \\ 0 \\ 0 \\ 0 \\ 0 \\ 0 \\ 0 \end{Bmatrix} \tag{38}$$

$\left[\widetilde{V}\right]$ is a 7×7 matrix with the eigenvectors as columns. The force-influence-functions in Laplace domain are obtained from Equation (38) and the Laplace transform of Equation (30). They are given by

$$\begin{Bmatrix} \overline{\mathrm{Q}}_{0,0}(x,s) \\ \overline{\mathrm{Q}}_{-1,1}(x,s) \\ \vdots \\ \overline{\mathrm{Q}}_{-1,0}(x,s) \end{Bmatrix} = \begin{Bmatrix} \overline{\mathrm{Q}}_1(x,s) \\ \overline{\mathrm{Q}}_2(x,s) \\ \vdots \\ \overline{\mathrm{Q}}_7(x,s) \end{Bmatrix} = E_f \left[\widetilde{V}\right] \begin{Bmatrix} a_1 \frac{-\sqrt{s\overline{G}_m(s)C\lambda_1}}{s}\exp\left[-\sqrt{s\overline{G}_m(s)C\lambda_1}\,x\right] \\ a_2 \frac{-\sqrt{s\overline{G}_m(s)C\lambda_2}}{s}\exp\left[-\sqrt{s\overline{G}_m(s)C\lambda_2}\,x\right] \\ \vdots \\ a_7 \frac{-\sqrt{s\overline{G}_m(s)C\lambda_7}}{s}\exp\left[-\sqrt{s\overline{G}_m(s)C\lambda_7}\,x\right] \end{Bmatrix} \tag{39}$$

and $\overline{\mathrm{Q}}_{n,m}(x,s) = 0$ for all n and m. As described in Section 2.1, Equations (17), (20), (22), (23) need to be evaluated at $s = 1/[2(t-t_k)]$. There are singularities in Equations (17), (20), (22), (23), and (39) at $t = t_k$, $k = 1\ldots r$. Hence, it is necessary to rewrite these equations to remove the singularities so that stresses and break opening-displacements can be computed even at the instants fiber fractures occur i.e. $t = t_k$, $k = 1\ldots r$.

The shear relaxation modulus can be written as a Prony series

$$G_m(t) = G_\infty + \sum_i G_i \exp\left(-\frac{t}{\tau_i}\right) \tag{40}$$

Taking the Laplace transform of Equation (40) and multiplying by s gives

$$s\,\overline{G}_m(s) = G_\infty + \sum_i \frac{G_i}{1+\dfrac{1}{s\tau_i}} \tag{41}$$

For $s = 1/[2(t-t_k)]$, Equation (41) becomes

$$\mathrm{B}(t-t_k) = \left\langle s\,\overline{G}_m(s)\right\rangle\Big|_{s=\frac{1}{2(t-t_k)}} = G_\infty + \sum_i \frac{G_i}{1+\dfrac{2(t-t_k)}{\tau_i}} \tag{42}$$

Evaluating Equation (39) at $s = 1/[2(t-t_k)]$ yields

$$\left\{\begin{array}{c}\overline{\mathrm{Q}}_{0,0}(x,s)\\ \overline{\mathrm{Q}}_{-1,1}(x,s)\\ \vdots\\ \overline{\mathrm{Q}}_{-1,0}(x,s)\end{array}\right\}\Bigg|_{s=\frac{1}{2(t-t_k)}} = 2(t-t_k)\left\{\begin{array}{c}\overline{\mathrm{q}}_{0,0}(x,s)\\ \overline{\mathrm{q}}_{-1,1}(x,s)\\ \vdots\\ \overline{\mathrm{q}}_{-1,0}(x,s)\end{array}\right\}\Bigg|_{s=\frac{1}{2(t-t_k)}} \tag{43}$$

where

$$\left\{\begin{array}{c}\overline{\mathrm{q}}_{0,0}(x,s)\\ \overline{\mathrm{q}}_{-1,1}(x,s)\\ \vdots\\ \overline{\mathrm{q}}_{-1,0}(x,s)\end{array}\right\}\Bigg|_{s=\frac{1}{2(t-t_k)}} = -E_f\sqrt{\mathrm{B}(t-t_k)C}\left[\widetilde{V}\right]\left\{\begin{array}{c}a_1\sqrt{\lambda_1}\exp\left(-\sqrt{\mathrm{B}(t-t_k)C\lambda_1}\,x\right)\\ a_2\sqrt{\lambda_2}\exp\left(-\sqrt{\mathrm{B}(t-t_k)C\lambda_2}\,x\right)\\ \vdots\\ a_7\sqrt{\lambda_7}\exp\left(-\sqrt{\mathrm{B}(t-t_k)C\lambda_7}\,x\right)\end{array}\right\} \tag{44}$$

and $\overline{\mathrm{q}}_{n,m}(x,s) = 0$ for all other n, m. It should be pointed out that in the final numerical solution of Equation (44) for $\overline{\mathrm{q}}_{n,m}(x,s)$ there is only one eigenmode because 5 of the 7 a_i's and one of the λ_i's are zero. Evaluating Equation (17) and (20) at $s = 1/[2(t-t_k)]$ gives the system of equations

$$0 = \sum_{j=1}^{L_k} \left\langle \overline{\mathrm{q}}_{n_i - n_j, m_i - m_j}\left(x_i - x_j, s\right)\right\rangle\Big|_{s=\frac{1}{2(t-t_k)}} \left\langle s\, \overline{u}^{k}_{n_j, m_j}\left(x_j, s\right)\right\rangle\Big|_{s=\frac{1}{2(t-t_k)}}, \text{ for } i = 1\ldots L_{k\text{-}1}$$

$$-\sigma^{t_{k-1}}_{n_i, m_i}\left(x_i, t\right) \approx \sum_{j=1}^{L_k} \left\langle \overline{\mathrm{q}}_{n_i - n_j, m_i - m_j}\left(x_i - x_j, s\right)\right\rangle\Big|_{s=\frac{1}{2(t-t_k)}} \times \left\langle s\, \overline{u}^{k}_{n_j, m_j}\left(x_j, s\right)\right\rangle\Big|_{s=\frac{1}{2(t-t_k)}}, \quad \text{for } i = L_{k\text{-}1} + 1\ldots L_k \tag{45}$$

Equation (45) represents L_k linear algebraic equations that are solved for the quantity $\left\langle s\, \overline{u}^{k}_{n_j, m_j}\left(x_j, s\right)\right\rangle$, $j = 1\ldots L_k$, at $s = 1/[2(t\text{-}t_k)]$. In order to obtain Equation (45), it is necessary to substitute Equation (29) into Equation (20). Finally, Equation (22) is rewritten as

$$\sigma^{t_k}_{n,m}\left(x,t\right) \approx \sigma^{t_{k-1}}_{n,m}\left(x,t\right) + \sum_{j=1}^{L_k} \mathrm{H}\left(t - t_k\right)\left[\overline{\mathrm{q}}_{n-n_j, m-m_j}\left(x - x_j, s\right)\left\langle s\, \overline{u}^{k}_{n_j, m_j}\left(x_j, s\right)\right\rangle\right]_{s=\frac{1}{2(t-t_k)}} \tag{46}$$

The final time-dependent solution procedure is as follows. Equation (45), (46), and (23) are solved recursively starting from $k = 1$ through $k = r$. Finally, the fiber stresses and break opening displacements due to the arbitrary sequence of breaks are given by Equation (1) and (2), respectively.

If the shear creep compliance $J_m(t)$, is available instead of $G_m(t)$ then $\mathrm{B}(t\text{-}t_k)$ needs to be redefined. The Prony series for the creep compliance is

$$J_m\left(t\right) = \frac{1}{G_0} + \sum_i \frac{1}{G_i}\left[1 - \exp\left(-\frac{t}{\tau_i}\right)\right] + \frac{t}{\eta_\infty} \tag{47}$$

Taking the Laplace transform of Equation (47) and multiplying by s gives

$$s\bar{J}_m\left(s\right) = \frac{1}{G_0} + \sum_i \frac{1}{G_i}\left[1 - \frac{1}{1 + \frac{1}{s\tau_i}}\right] + \frac{1}{s\eta_\infty} \tag{48}$$

$\bar{J}_m(s)$ and $\overline{G}_m(s)$ are related by

$$s\overline{G}_m(s) = \frac{1}{s\bar{J}_m(s)} \tag{49}$$

Hence,

$$\mathrm{B}(t-t_k) = \left\langle \frac{1}{s\bar{J}_m(s)} \right\rangle \Bigg|_{s=\frac{1}{2(t-t_k)}} = \frac{1}{\frac{1}{G_0} + \sum_i \frac{1}{G_i}\left[1 - \frac{1}{1+\frac{2(t-t_k)}{\tau_i}}\right] + \frac{2(t-t_k)}{\eta_\infty}} \tag{50}$$

2.3 *Time-Dependent HVDLS*

In order to implement the HVDLS, it is necessary to develop a new set of $\overline{\mathrm{q}}_{n,m}(x,s)$ for x = [0, x_p]. Consider regular hexagonal fiber packing as shown in Figure 1. The displacement of fiber (n, m), at axial position x, is denoted by $v_{n,m}(x)$. Equation (51) is the system of equation for fiber displacements obtained under shear-lag assumptions.

$$\begin{aligned}\frac{\partial^2 v_{n,m}}{\partial x^2} + C\int_0^t G_m(t-\beta)\frac{\partial}{\partial\beta}\big[&v_{n+1,m}(x,\beta) + v_{n,m+1}(x,\beta) + v_{n-1,m}(x,\beta) + v_{n,m-1}(x,\beta) \\ &+ v_{n+1,m-1}(x,\beta) + v_{n-1,m+1}(x,\beta) - 6v_{n,m}(x,\beta)\big]\mathrm{d}\beta = 0 \ , \ \text{for all } n, m\end{aligned} \tag{51}$$

The boundary conditions for calculating influence-functions are

$$\begin{aligned} &v_{0,0}(0,t) = \mathrm{H}(t); \\ &v_{n,m}(0,t) = 0 \ \text{ for all } n, m \text{ other than } n = m = 0 \text{ and } t \geq 0 \\ &\text{and } \left.\frac{\partial v_{n,m}(x,t)}{\partial x}\right|_{x=\infty} = 0 \text{, for all } n, m \text{ and } t \geq 0 \end{aligned} \tag{52}$$

and the initial conditions are

$$v_{n,m}(x,0) = 0 \text{ , for all } n, m \text{ and } x = [0, \infty] \tag{53}$$

The Laplace transform of Equations (51) and (52) is

$$\frac{\mathrm{d}^2\bar{v}_{n,m}}{\mathrm{d}x^2} + sC\overline{G}_m\left[\bar{v}_{n+1,m} + \bar{v}_{n,m+1} + \bar{v}_{n-1,m} + \bar{v}_{n,m-1} + \bar{v}_{n+1,m-1} + \bar{v}_{n-1,m+1} - 6\bar{v}_{n,m}\right] = 0 \ \text{ for all } n, m \tag{54}$$

with boundary conditions

$$\bar{v}_{0,0}(0,s) = 1/s;$$

$$\bar{v}_{n,m}(0,s) = 0, \text{ for all } n, m \text{ other than } n = m = 0$$

$$\text{and } \left.\frac{\partial \bar{v}_{n,m}(x,s)}{\partial x}\right|_{x=\infty} = 0, \text{ for all } n, m \tag{55}$$

Equation (54) is solved by applying the discrete Fourier transform given by

$$\bar{v}_{n,m}(x,s) = \sum_{l=0}^{N-1}\sum_{j=0}^{M-1} \tilde{v}(x,s,l,j) \exp\left(-\frac{2\pi \hat{i} l n}{N}\right) \exp\left(-\frac{2\pi \hat{i} j m}{M}\right) \tag{56}$$

$$\text{where } \hat{i} = \sqrt{-1}$$

The inverse Fourier transform is given by

$$\tilde{v}(x,s,l,j) = \frac{1}{NM}\sum_{n=0}^{N-1}\sum_{m=0}^{M-1} \bar{v}_{n,m}(x,s) \exp\left(\frac{2\pi \hat{i} l n}{N}\right) \exp\left(\frac{2\pi \hat{i} j m}{M}\right) \tag{57}$$

Applying the Fourier transform implies periodicity in the n and m directions. Hence, the state of fiber (n, m), at location x, is the same as the state of fiber (n+N, m+M), at location x. Substituting Equation (56) into Equations (54) and (55) yields

$$\frac{\mathrm{d}^2\tilde{v}}{\mathrm{d}x^2} + sC\,\bar{G}_m\,\tilde{v}\left[2\cos\left(\frac{2\pi l}{N}\right) + 2\cos\left(\frac{2\pi j}{M}\right) + 2\cos\left(\frac{2\pi l}{N} - \frac{2\pi j}{M}\right) - 6\right] = 0 \tag{58}$$

with boundary conditions

$$\tilde{v}(0,s,l,j) = \frac{1}{sNM} \text{ and } \left.\frac{\mathrm{d}\tilde{v}(x,s,l,j)}{\mathrm{d}x}\right|_{x=\infty} = 0 \tag{59}$$

The solution to Equations (58) and (59) is given by

$$\tilde{v} = \frac{1}{sNM}\exp\left\{-\sqrt{sC\bar{G}_m\left[6 - 2\cos\left(\frac{2\pi l}{N}\right) - 2\cos\left(\frac{2\pi j}{M}\right) - 2\cos\left(\frac{2\pi l}{N} - \frac{2\pi j}{M}\right)\right]}\,x\right\} \tag{60}$$

Substituting Equation (60) into Equation (56) yields

$$\bar{v}_{n,m}(x,s) = \frac{1}{sNM}\sum_{l=0}^{N-1}\sum_{j=0}^{M-1}\left\langle \exp\left\{-\sqrt{sC\bar{G}_m\left[6 - 2\cos\left(\frac{2\pi l}{N}\right) - 2\cos\left(\frac{2\pi j}{M}\right) - 2\cos\left(\frac{2\pi l}{N} - \frac{2\pi j}{M}\right)\right]}\,x\right\} \times \exp\left[-\frac{2\pi \hat{i} l n}{N}\right]\exp\left[-\frac{2\pi \hat{i} j m}{M}\right]\right\rangle \tag{61}$$

Finally, the force influence-functions in Laplace domain are given by

$$\overline{\mathrm{Q}}_{n,m}(x,s) = E_f \frac{\partial \overline{v}_{n,m}(x,s)}{\partial x} \tag{62}$$

The differences between NNLS and HVDLS are apparent in the solution approaches. Equation (61) is the solution to a coupled system of *NM* ordinary differential equations given by Equations (54) and (55). The NNLS is obtained by solving a set of seven coupled ordinary differential equations for the broken fiber and its nearest six neighbors as shown in Section 2.2.

For HVDLS the quantity $\overline{\mathrm{q}}_{n,m}(x,s)$ in Equations (45) and (46) is

$$\begin{aligned}\overline{\mathrm{q}}_{n,m}\big|_{s=\frac{1}{2(t-t_k)}} = & \frac{E_f}{NM} \\ & \times \sum_{l=0}^{N-1}\sum_{j=0}^{M-1}\left\langle \exp\left\{-\sqrt{\mathrm{B}(t-t_k)C\left[6-2\cos\left(\frac{2\pi\, l}{N}\right)-2\cos\left(\frac{2\pi\, j}{M}\right)-2\cos\left(\frac{2\pi\, l}{N}-\frac{2\pi\, j}{M}\right)\right]}\, x\right\}\right. \\ & \times\left(-\sqrt{\mathrm{B}(t-t_k)C\left[6-2\cos\left(\frac{2\pi\, l}{N}\right)-2\cos\left(\frac{2\pi\, j}{M}\right)-2\cos\left(\frac{2\pi\, l}{N}-\frac{2\pi\, j}{M}\right)\right]}\right) \\ & \left.\times\exp\left[-\frac{2\pi\,\hat{i}\, l\, n}{N}\right]\exp\left[-\frac{2\pi\,\hat{i}\, j m}{M}\right]\right\rangle\end{aligned} \tag{63}$$

where $\mathrm{B}(t\text{-}t_k)$ is given by Equation (42) or Equation (50) for shear relaxation modulus or creep compliance, respectively. Similar to Equation (43)

$$\overline{\mathrm{Q}}_{n,m}(x,s)\big|_{s=\frac{1}{2(t-t_k)}} = 2(t-t_k)\,\overline{\mathrm{q}}_{n,m}(x,s)\big|_{s=\frac{1}{2(t-t_k)}} \tag{64}$$

2.4 *Time-Dependent Load Sharing Based on Finite Elements*

It is possible to generate force influence-functions in Laplace domain by finite element analysis of a single fractured fiber surrounded by one or more hexagonally packed rings of neighboring fibers. Bandorawalla *et. al.* (2002b) developed this approach for quasi-static NNLS. For time-dependent force influence-functions, a transient finite element analysis with linearly elastic fiber properties and linearly viscoelastic matrix properties would be required. Displacement boundary conditions would be applied in the fiber direction to produce a far-field axial strain of $\varepsilon_{ff}\,\mathrm{H(t)}$ in the fibers. Time-dependent axial fiber stresses $\sigma_{n,m}^{\mathrm{fem}}(x,t)$, would then be calculated for the broken and neighboring fibers. Let the broken fiber be designated (0, 0) and the fracture be in

the x = 0 plane. The time dependent break opening-displacement $u^{\text{fem}}(t)$, of the single fiber fracture would also be available from the finite element analysis. $\sigma_{n,m}^{\text{fem}}(x,t)$ and $u^{\text{fem}}(t)$ could be fit to a Prony series. The Laplace transform of these two quantities are related by

$$\overline{\sigma}_{n,m}^{\text{fem}}(x,s) = \frac{\sigma_{ff}}{s} + \overline{\mathrm{Q}}_{n,m}(x,s)\, s\, \overline{u}^{\text{fem}}(s) \tag{65}$$

from which $\overline{\mathrm{Q}}_{n,m}(x,s)$, and hence $\overline{\mathrm{q}}_{n,m}(x,s)$, could be calculated. The difficulties associated with calculating influence-functions in Laplace domain by the finite element method outlined above are:

1. Sufficient mesh refinement for spatial convergence of results.
2. Sufficiently small increments in time for temporal convergence of results.
3. Accounting for residual thermal stresses due to cure shrinkage in the macromodel composites if quantitative comparison is to be made to time-dependent load-sharing measurements of Bandorawalla *et. al.* (2002a).

For the reasons cited above, the shear-lag load-sharing techniques described in Sections 2.2 and 2.3 are used for the stress-rupture lifetime predictions made in this paper.

3 COMPARISON BETWEEN NNLS AND HVDLS

Representative stress profiles in neighboring fibers caused by an isolated break in fiber (0, 0) at x = 0 are shown in Figure 8 through Figure 11. The axial location along the fiber is expressed in terms of the fiber radius, r_f. Under NNLS only the stress in the nearest neighbor is perturbed as shown in Figure 8. Although the far-field fiber stress is held constant, matrix viscoelasticity causes the overloaded length on unbroken fibers adjacent to a fiber fracture location to increase with time. Consequently, there is a greater probability of fiber failure occurring in these unbroken fibers. This time-dependent fiber stress redistribution is the primary cause of failure in a unidirectional polymer matrix composite under longitudinal stress-rupture loading. Similar trends in the time dependence of stresses calculated by HVDLS are seen in Figure 9 through Figure 11. The HVDLS results are computed for a 10□10 array of hexagonally packed fibers. HVDLS predicts a lower peak stress concentration than NNLS in the fibers closest to the fractured fiber. However, the HVDLS approach also produces a small perturbation of the stresses in the next to nearest neighbors as shown in Figure 10 and Figure 11. The peak stress

concentration on the next to nearest neighboring fibers is much smaller than on the nearest neighbors. An important consequence of shear-lag assumptions is that the peak stress concentration due to an isolated fiber fracture does not change with time. In fact this peak stress concentration is not a function of any geometric or material properties of the composite if regular hexagonal fiber packing is assumed. It should also be pointed out that since under shear-lag assumptions the matrix does not carry any normal tensile stress there is no provision in the analysis to account for an increase in the far-field fiber stress with time due a viscoelasticity-based decrease of the tensile load carried by the matrix. This is not a serious source of error since for most polymer matrix composites with high fiber volume fractions and high fiber to matrix stiffness ratios the total tensile load carried by the matrix is negligible.

The stresses in the broken fiber decrease with time as shown in Figure 12. Although Figure 12 shows stresses calculated by NNLS, very similar curves are obtained for HVDLS. It is unlikely for another break to occur in the under-stressed region of a broken fiber. Hence, the decrease of axial stress in a broken fiber with time is not the controlling mechanism for stress-rupture failure in unidirectional polymer composites.

Bandorawalla *et. al.* (2002a) made in-situ fiber strain concentration measurements in macromodel composites with fibers that were large enough that strain gages could be mounted directly onto the surface of the fibers. The time-dependent strain concentration measurements agreed with the trends described in this paper for both the broken fibers and the unbroken neighbors. Representative measurements on unbroken neighboring fibers with two adjacent coplanar fiber fractures are shown in Figure 13. The axial positions of the gages referenced to the plane of fiber fractures are denoted by x in Figure 13. The presence of multiple adjacent fiber fractures produces a more pronounced change in strain concentration with time than for an isolated fiber fracture. The model composite measurements provide a qualitative verification for the load sharing philosophy described in Section 2. A detailed time-dependent finite element analysis of the model composite domain is necessary to make a quantitative comparison between the measurements and modeling approach. The finite element model could then be used to establish whether NNLS or HVDLS is more appropriate for modeling time-dependent micromechanical stress redistribution in unidirectional composite materials. This procedure was

followed by Bandorawalla *et. al.* (2002b) to investigate the applicability of shear-lag models for quasi-static load sharing.

4 STRESS-RUPTURE LIFETIME MODELING

A Monte Carlo simulation is used to predict the stress-rupture lifetime of a unidirectional composite material. Micromechanical stress redistribution can be calculated by applying either the NNLS or HVDLS described in Section 2. Initial rupture lifetimes are measured on a unidirectional carbon fiber/polymer matrix composite. The difficulties associated with measuring rupture lifetimes of unidirectional systems are discussed, and rupture lifetimes are obtained for an alternate material system with 90° plies on the surface. Comparisons between the simulation predictions and lifetime measurements on the alternate material system are presented.

4.1 *Rupture Simulation Approach*

Failure of unidirectional composite materials loaded in tension in the fiber direction is controlled by failure of fibers. The stochastic simulation approach attempts to track the progression of fiber fractures leading to eventual composite failure. All material property inputs to the simulation other than the fiber strength are assumed to be deterministic. A Weibull distribution given by

$$P_f(\sigma, l) = 1 - \exp\left[-\frac{l}{l_o}\left(\frac{\sigma}{\sigma_o} \right)^m \right] \tag{66}$$

describes the probability of failure P_f, of a fiber of length l, at a stress level σ. σ_o is the Weibull location parameter, and m is the fiber Weibull modulus or shape parameter. σ_o is interpreted as the stress level required to cause one failure on average in a fiber of length l_o. m is related to the variability in fiber strength, with a higher m for a narrower distribution. Weibull parameters for the strength distribution of certain fibers are available in the literature (e.g. Wimolkiatisak and Bell, 1989).

An outline of the stress-rupture simulation procedure and the representative volume of material with fibers and matrix is shown in Figure 14. Uniform hexagonal fiber packing is assumed. In order to track the location of fiber fractures every fiber is subdivided into the same number of

elements along its length as shown in Figure 14. A fracture is allowed to occur at a random location within each fiber element. Landis *et. al.* (2000) have reported that positioning a break at random within a fiber element significantly reduces the number of elements along each fiber required for convergence of the simulation results. Values of strength are assigned to the fiber elements by using the Weibull strength distribution of Equation (66). While the distribution of fiber strength remains the same, the actual element strengths change for every computation of rupture lifetime. To begin the simulation process, the far-field axial fiber stress σ_{ff}, is increased to the fiber stress level at which rupture lifetimes are desired i.e. $\sigma_{ff}^{\text{rupt}}$. This initial ramp up is assumed to occur instantaneously, and depending on the rupture stress level may result in fiber element failures. During the initial ramp up, fiber stress redistribution is calculated by applying the quasi-static version of load sharing using the instantaneous matrix modulus since ramp up is assumed to be instantaneous and hence matrix viscoelasticity does not play a role. The general time-dependent load sharing framework is easily specialized to determine the instantaneous stress redistribution. This is achieved by using Equations (45), (46), (23), (1), and (2) to compute fiber stresses at $t = 0$ due to a single set of b_1 breaks that occur simultaneously at $t_1 = 0$. The ramp up is carried out by increasing the far-field stress to cause failure of the next weakest element only if no further fiber element failures occur due to stress redistribution at the current far-field stress level. Once $\sigma_{ff}^{\text{rupt}}$ is attained, the far-field fiber stress is held constant and the time level is incremented to cause failure of fiber elements. The mechanism for tensile stress rupture of unidirectional polymer composites is discussed in Section 3. The time level is incremented in a geometric progression to maximum of $t = t_{\max}$. This results in a linear increase in time on a logarithmic scale. At each new time level fiber stresses are computed and a check is performed for further fiber element failures. If a fiber failure is detected at a current time level, it is assumed to have occurred at an intermediate time halfway between the previous time level and the current time level. Following the notation developed in Section 2.1, the most recent fiber failures occur at t_r. Local stress redistribution may result in further fiber element failures at the same time level. These additional failures are assumed to occur at t_r, and hence, b_r may increase due to stress redistribution alone. The time level is incremented only after no further fiber element failures occur at the same time level. The process is repeated until the surviving fiber elements in a cross-section of the simulation volume can no longer sustain the global load i.e.

stress rupture material failure is predicted. The time level at this point is the calculated rupture lifetime of the simulation volume. It is also possible that stress rupture failure does not occur by t_{max}, in which case a runout is predicted. In order to expedite the simulation process two techniques are implemented:

1. If all the fiber elements are intact after the initial ramp up, then the time-dependent load-sharing framework described in Section 2 will not predict any change in fiber stresses with time, and hence, no fiber element failures at all. This is a consequence of assuming that the fibers are linearly elastic and that the matrix is capable of sustaining only shear stresses. Hence, it is not necessary to progressively increase the time level as a runout will be predicted if no fiber element failures occur during the initial ramp up.
2. Even if a few fiber failures do occur during the initial ramp up, no additional fiber fractures may occur in t_{max} due to time-dependent fiber stress evolution. This is very easily checked by directly computing the stresses at t_{max} due to only those fiber fractures that occur during the initial ramp up. If the stresses at t_{max} are not large enough to cause failure of any additional fiber elements then a runout is predicted without having to progressively increase the time level.
3. A single set of $\bar{q}_{n,m}(x,s)\big|_{s=1/2t}$ is calculated for all (n, m) at a discrete number of points over $t = [0, t_{max}]$ and $x = [0, x_p]$. $\bar{q}_{n,m}(x,s)\big|_{s=1/2t}$ is computed at equally spaced axial positions over $x = [0, x_p]$. The temporal variation is obtained by computing $\bar{q}_{n,m}(x,s)\big|_{s=1/2t}$ at $t = 0$ and for additional equally spaced times on a logarithmic scale over $t = (0\ t_{max}]$. Linear interpolation in x and the logarithm of t is used to determine $\bar{q}_{n,m}(x,s)\big|_{s=1/2t}$ at an arbitrary axial position and time, respectively.

Before the simulation procedure described above can be used to obtain lifetimes the far-field fiber stress level σ_{ff}^{rupt} needs to be established. The first step in this process is to compute the composite strength distribution of the simulation volume (Bandorawalla *et. al.*, 2002b). This is achieved by ramping up the far-field fiber stress instantaneously and calculating fiber stress redistribution with the quasi-static version of load sharing as described earlier in this section. The composite strength of the simulation volume corresponds to the far-field fiber stress at

which all the fiber elements in a cross-sectional plane fail. 100 strengths are computed in this manner. The computed composite strengths of the simulation volume conform to a Weibull distribution with a location and shape parameter given by $\tilde{\sigma}_o^{\text{sim}}$ and $\tilde{m}^{\text{sim}}$, respectively. The second step in establishing $\sigma_{ff}^{\text{rupt}}$ is to measure strengths of the composite material under consideration. The experimental composite strengths conforms to a Weibull distribution with location and shape parameter $\tilde{\sigma}_o^{\text{exp}}$ and $\tilde{m}^{\text{exp}}$, respectively. The experimental rupture lifetimes are measured at a composite stress level of $R^{\text{exp}}\tilde{\sigma}_o^{\text{exp}}$. The composite stress level for performing the rupture simulations is $R^{\text{sim}}\tilde{\sigma}_o^{\text{sim}}$. R^{sim} is calculated by equating the experimental instantaneous probability of failure of the composite at $R^{\text{exp}}\tilde{\sigma}_o^{\text{exp}}$ to the instantaneous probability of failure of the simulation volume at $R^{\text{sim}}\tilde{\sigma}_o^{\text{sim}}$. Thus,

$$P_f = 1 - \exp\left[-\left(R^{\text{exp}}\right)^{\tilde{m}^{\text{exp}}}\right] = 1 - \exp\left[-\left(R^{\text{sim}}\right)^{\tilde{m}^{\text{sim}}}\right] \tag{67}$$

Finally, the far-field fiber stress level for the rupture simulation is given by

$$\sigma_{ff}^{\text{rupt}} = \frac{R^{\text{sim}}\tilde{\sigma}_o^{\text{sim}}}{V_f} \tag{68}$$

4.2 *Material Systems*

Initial measurements of rupture lifetime are made on a Grafil 34-700 standard modulus/polyphenylene sulfide (PPS) pultruded unidirectional composite tape. The experimental composite strengths of the Grafil carbon fiber/PPS composite conform to a Weibull distribution with $\tilde{\sigma}_o^{\text{exp}}$ = 1.57 GPa and $\tilde{m}^{\text{exp}}$ = 29.4 at a gage length $\tilde{l}_o$ = 76 mm. The composites have a fiber volume fraction V_f, of 40%. The experimental rupture lifetimes of the Grafil carbon fiber/PPS composite are shown in Figure 15. When the stress rupture simulation was used to predict lifetime, two significant inconsistencies between experimental lifetimes and the predictions were observed:

1. The simulation methodology over-predicted stress rupture lifetimes, and
2. The rupture lifetime predictions had much greater variability than the experimental lifetimes.

Measuring the tensile strength and rupture lifetime of purely unidirectional composite materials poses certain challenges. Although the specimens are tabbed as shown in Figure 16, the application of grip pressure unavoidably causes material damage and fiber fractures in the gripped section of the specimen. The time-dependent propagation of these defects in the grip section during stress rupture loading dominates the failure behavior of purely unidirectional specimens. The tabbing materials used consisted of 100-count (100 wires per linear inch) stainless steel screen and 1000 series aluminum sheet that was 0.02 inches thick. A piece of screen is folded in half over the ends of the specimen, and an aluminum piece is folder over the screen on the ends of the specimen as shown in Figure 16. It is difficult to adhesively bond tabbing material such as Grade G-10 Garolite woven glass fiber laminates to a PPS-based composite. Even with adhesively bonded tabs failures were observed in or near the gripped section due to a high stress concentration.

In order to alleviate the problems caused by grip-induced damage stress-rupture lifetimes are measured on an alternate material system with 90° external plies. Composite panels with a $[90/0_3]_s$ layup are compression molded from APC-2 prepreg supplied by Cytec Industries. APC-2 prepreg consists of AS4 carbon fiber with a thermoplastic polyetheretherketone (PEEK) matrix. The specimens have a fiber volume fraction of 54% and a gage length of 76 mm with a rectangular cross-section of 1 mm × 12.7 mm, nominally. The tabbing method described earlier in this section is used to test the APC-2 composite. However, a finer 200-count (200 wires per linear inch) stainless steel screen was used instead of the 100-count screen. The finer tabbing screen and the 90° external plies protect the load carrying 0° plies from damage in the gripped section. Figure 17 shows a typical failed Grafil/PPS unidirectional specimen along with a typical failed APC-2 $[90/0_3]_s$ specimen. While it is difficult to pinpoint where initial and ultimate failure occurred in the Grafil/PPS unidirectional specimens, all the APC-2 $[90/0_3]_s$ specimens consistently failed in the gage section. In Section 5 the stress-rupture models described in this paper will be used to reiterate why it is necessary to prevent grip-induced damage for reliable rupture lifetime measurements.

The relative stiffness of the 0° and 90° laminae in the direction of the tensile load is used to determine that each of the 90° plies carry approximately 1.7% of the total load on the $[90/0_3]_s$

laminate. Hence, it can safely be assumed that the contribution of the 90° plies to the strength and lifetime of the laminate is negligible.

Two batches of the APC-2 laminate are fabricated. Although both batches had the same fiber volume fraction and lay-up, very different strength distributions are measured as shown in Table 1. The reason for this inconsistency is not clear, although, it may be the result of unintended differences in the temperature cycle during processing. The quasi-static strengths of the APC-2 specimens are measured at two temperatures: 125°C and 140°C. All the tests are performed by using a Material Testing System (MTS) servohydraulic machine. The strengths are measured with a loading rate of 445 N/sec. Since the primary interest is rupture lifetimes, very few specimens are used to measure quasi-static strength. The quasi-static strength of only three specimens is measured at each temperature for the Weibull parameters of Batch I. The quasi-static strength of five specimens is measured at each temperature for the Weibull parameters of Batch II. The rupture lifetimes of the APC-2 specimens are also measured at two temperatures: 125°C and 140°C. The load profile for the tensile rupture tests consists of an initial ramp at 445 N/sec and a subsequent hold at the desired load. All the lifetime measurements from both Batch I and Batch II are displayed in Figure 18. However, because of the marked difference in the strength of Batch I and Batch II they are treated separately when calculating $R^{\exp}$ in Figure 18. The test is stopped after approximately 4 days, and any specimen that does not fail in that period of time is treated as a runout. The data points corresponding to instantaneous failures in Figure 18 are placed at 0.1 seconds. It is immediately apparent that there is a very large variability in rupture lifetimes at each stress level. Hence, it is very important that a life prediction technique be stochastic in nature, and be able to compute material reliability at a given stress level and temperature. It will be shown that the Monte Carlo simulation technique described here is particularly well suited to do this.

However, the experimental results for rupture lifetime shown in Figure 18 (and the simulation predictions shown later) should always be interpreted in light of the quasi-static strength distribution for two important reasons. Firstly, the strength distribution can be used to establish the probability of instantaneous failure at a given rupture stress level. Secondly, a material system with greater variability in quasi-static strength may intuitively be expected to possess a

greater variability in stress-rupture lifetime. For example, there is a significant variability in the quasi-static strength distribution for Batch II that may translate into greater variability in rupture lifetime measurements for Batch II (although in Section 5 it is shown that the strength-life equal rank assumption does not hold for longitudinally loaded unidirectional polymer composites).

The fiber strength statistics, fiber stiffness and geometry, and the viscoelastic shear properties of the matrix are required to implement the stress rupture simulation described in Section 4.1. Wimolkiatisak and Bell (1989) have studied the strength of Hercules AS4 carbon fibers using the single-fiber fragmentation test. Their data can be used to calculate the following parameters for the Weibull strength distribution of AS4 carbon fibers: $\sigma_o = 5.25$ GPa, $l_o = 1$ mm, and $m = 10.65$. The axial Young's modulus of AS4 carbon fibers $E_f = 234.4$ GPa, and the fiber radius $r_f = 3.5$ μm. The shear creep compliance master curve and shift factors shown in Figure 19 are generated from short term creep data of neat PEEK at several temperatures. Flexural mode creep tests were conducted in a TA Instruments Dynamic Mechanical Analyzer (DMA) 2920. It should be pointed out that approximate shear properties are calculated from flexural mode tests in a DMA. Figure 19 gives the shear creep compliance of PEEK over several decades of time at any temperature from 124°C to 205°C. With this information predictions of rupture lifetime can be obtained at any temperature from 124°C to 205°C. Hence, the simulation technique described here can be used to understand and predict the role of temperature in accelerated measurement of stress-rupture lifetimes.

4.3 *Stress-Rupture Simulation Results*

The Monte Carlo simulation approach is used to predict stress rupture lifetimes of the APC-2 composite at 125°C and 140°C. The material properties described in Section 4.2 are used for the lifetime predictions.

As mentioned earlier, the first step is to compute a quasi-static strength distribution. The strength distribution is required at both 125°C and 140°C. The specialization of load-sharing described in Section 4.1 for instantaneous ramp up would not predict different quasi-static strengths at different temperatures since it is based on the instantaneous shear compliance of the

matrix. For temperature dependent strength predictions, it is necessary consider finite ramp up rates with temperature and time dependent viscoelastic shear properties for the matrix material. The general load-sharing approach developed in Section 2 cannot be easily modified to account for a finite ramp rate α, in the far-field fiber stress, because the Laplace inversion approximation given by Equation (5) is developed for problems where all inputs are step-functions in time applied at $t = 0$ (Schapery, 1967). An approximation is used to compute load sharing with a finite ramp rate for far-field fiber stress. The stresses at time t are computed by treating the far-field stress $\alpha\, t$ as if it were a step-function in time applied at $t = 0$ i.e. $\sigma_{ff}^{\text{rupt}} = \alpha\, t\, \mathrm{H}(t)$. With this technique it is possible to use time and temperature dependent matrix shear properties to compute temperature dependent quasi-static strength distributions. However, the loading rate of 445 N/sec is high enough that time and temperature depend matrix deformation does not play a significant role in the strength predictions and the same strength distribution is computed at both temperatures. 100 strength computations are performed on a simulation volume consisting of a 10×10 array of fibers with axial length $X = 0.47$ mm. The Weibull parameters obtained from the 100 strength values are shown in Table 2. Different strength distributions are obtained by applying NNLS and HVDLS. It should be pointed out that $\tilde{\sigma}_o^{\text{sim}}$ is computed for unidirectional APC-2, while the strengths reported in Table 1 are for the $[90/0_3]_s$ laminate. Since the 90° plies may be assumed to carry no load, $\tilde{\sigma}_o^{\text{sim}}$ for the $[90/0_3]_s$ laminate may be assumed to be $3/4^{\text{th}}$ of the values reported in Table 2.

Figure 20 through Figure 23 show rupture lifetime predictions for the APC-2 material. All the rupture lifetime predictions are performed with a $t_{\max}$ of 4 days. The simulation volume consisting of a 10×10 array of fibers with axial length $X = 0.47$ mm.

Figure 20 and Figure 21 are the rupture lifetimes predictions at 125°C and 140°C, respectively, calculated with NNLS. The rupture lifetime predictions are plotted along with the experimental results. At each R^{exp}, 100 rupture lifetimes are comsputed. The numbers displayed with the symbol '←' represent experimental and predicted instantaneous failures. The symbol '→' and its associated number represent experimental and predicted runouts in 4 days. The number of measured and predicted runouts may be regarded as the experimental and predicted reliability of

the material to withstand the given stress level and temperature for a desired lifetime of 4 days. The horizontal brace and its associated number refer to the measured and predicted rupture failures that occur within 4 days. R^{sim}, and hence, the far-field fiber stress level for the rupture simulation is calculated by equating the experimental probability of instantaneous failure with the probability of instantaneous failure for the simulation volume as given by Equation (67). The number of instantaneous failures predicted by the simulation as a fraction of 100 is approximately equal to the probability of instantaneous failure at each stress level and temperature. Since more experimental measurements are made for Batch II, a complete comparison is obtained at the lower R^{exp} in Figure 20 and Figure 21. The simulations predict more runouts at the lower temperature of 125°C than at 140°C. Consequently, far fewer rupture failures are predicted at 125°C than at 140°C. Although, the experimental measurements are limited, they appear to have a similar trend of longer lifetimes at 125°C than at 140°C. It is encouraging to note that at fraction of instantaneous failures, rupture failures in 4 days, and runouts show a close correlation between the measurements and predictions at 140°C and the lower R^{exp}.

Similarly, the rupture lifetimes computed with HVDLS at 125°C and 140°C are shown in Figure 22 and Figure 23, respectively. The HVDLS also predicts longer lifetimes at lower temperatures. Comparing the rupture lifetimes obtained by NNLS and HVDLS, it appears as if the HVDLS technique predicts shorter lifetimes. As explained in Section 3, for HVDLS a single fractured fiber perturbs the stresses in all the neighboring fibers and there is an increase in the overstressed region of all the unbroken fibers with time. For NNLS, only the stresses in the nearest unbroken neighbors is perturbed due to single fractured fiber. Hence, stress rupture lifetimes computed with NNLS are longer than lifetimes computed with HVDLS.

5 VARIABILITY IN RUPTURE LIFETIME PREDICTIONS

Figure 24 shows a simple composite lamina consisting three parallel fibers. The figure attempts to illustrate the differences in the progression of fiber fractures leading to ultimate failure when the stress level is continually increased (as with strength measurement) and when the stress level is held constant (as with stress-rupture lifetime measurement). With quasi-static strength measurement the far-field stress level is continually increased, and hence, the critical cluster of

fiber fractures that ultimately causes failure of the material is not confined to a specific location. However, under stress-rupture conditions further fiber failures can only occur in the immediate vicinity of the initial fiber fractures caused by the rapid ramp-up to the desired creep level (see Section 3). In fact, if shear-lag assumptions are valid, fiber fractures will not occur in the zone of material where there are no initial fractures. Hence, it is apparent that the stress-rupture lifetime is very sensitive to the initial fiber fractures caused by the stress ramp-up, since these initial fiber fractures are the sites that nucleate further fiber failures with time. The computed rupture lifetime distribution is largely dictated by two factors:

1. The number of fiber element failures after the initial ramp-up, and
2. the strengths of the fiber elements in the neighborhood of these initial failure locations.

The above discussion serves to reiterate how important it is to ensure that no initial fiber damage is produced in the gripped section when measuring the stress-rupture lifetime of unidirectional polymer composite specimens. If initial fiber damage is produced in the gripped section of the specimen all subsequent fiber fractures will necessarily occur in the gripped section. Moreover, for a larger number of contiguous initial fiber fractures in the gripped section the measured lifetimes will be shorter and have a narrower distribution.

The strength-life equal rank assumption states that a statistically stronger specimen will have a longer lifetime. Although the strength-life equal rank assumption is intuitive and is often used to simplify life prediction modeling efforts, it cannot be experimentally proved or disproved. The Monte Carlo simulation technique can be used to show that the strength-life equal rank assumption does not hold for longitudinally loaded unidirectional polymer composites, since a different sequence of fiber fractures leads to ultimate failure under quasi-static and time-dependent conditions. This difference in the sequence of fiber fractures can be studied by assigning the same set of strengths to the fiber elements to compute a composite strength and a composite lifetime. Also, by computing several such sets of composite strengths and lifetimes it can be shown that there is no direct correlation between initial strength and lifetime.

In this section, the authors also investigate the reasons for large variability in computed lifetimes three different sets of input parameters are studied as described below. A total of 100 rupture

lifetimes are computed for each set of input parameters. All the results obtained in this section are computed by applying NNLS.

5.1 *Case I: Control Case*

The first set of input parameters is the same as the geometric and material parameters for the APC-2 composite at 140°C given in Section 4.2. This is the control case. However, for the results presented in this section $t_{\max}$ is increased to 3.1×10^{18} sec so that a more complete distribution of rupture lifetimes is calculated as shown in Figure 25. The results displayed in Figure 25 are calculated with a far-field fiber stress level $\sigma_{ff}^{0.5}$, which corresponds to a 50% probability of instantaneous failure.

5.2 *Case II: Narrower Fiber Strength Distribution*

The rupture lifetimes shown in Figure 26 are calculated with all the same input parameters as the control case except for the Weibull shape parameter for fiber strength which is changed from m = 10.65 to m = 25.0. This corresponds to a narrower fiber strength distribution than the control case. The results displayed in Figure 26 are also calculated with a far-field rupture stress level $\sigma_{ff}^{0.5}$, which corresponds to a 50% probability of instantaneous failure. It is apparent that longer rupture lifetimes with greater variability are computed with m = 25.0. Increasing the Weibull shape parameter for fiber strength from m = 10.65 to m = 25.0 does not change the composite strength distribution significantly. Hence, the far-field fiber stress level for rupture $\sigma_{ff}^{0.5}$, is essentially unchanged. $\sigma_{ff}^{0.5}$ is at the tail end of the fiber strength distribution, and since the Case II fibers have a much narrower strength distribution, fewer fiber element failures occur due to the instantaneous ramp up than in Case I. This results in longer rupture lifetimes, and greater variability in the computed lifetimes.

5.3 *Case III: Shorter Perturbed Axial Length Due to Fiber Fracture*

For this case, a combination of geometric and material parameters is altered from its value in the control case. The factor $\mathrm{B}(t-t_k)C$ in Equation (44) is related to the perturbed length along the broken or neighboring fiber due to a fiber fracture. B(t-t_k) is essentially the shear relaxation

modulus of the matrix $G_m(t\text{-}t_k)$, and C is related to the fiber radius, fiber volume fraction, and fiber axial modulus as given by Equation (32). $B(t-t_k)C$ is changed to 4 times its value in the control case which has the effect of halving the perturbed axial length at all times. As with the previous two cases, the rupture simulation is performed at a far-field rupture stress level $\sigma_{ff}^{0.5}$, which corresponds to 50% probability of instantaneous failure. As shown in Figure 27, there is no significant change in the computed lifetime distribution calculated by increasing $B(t-t_k)C$ to 4 times its control value. Similar results are obtained by increasing $B(t-t_k)C$ to 9 times its control value. These results may be counterintuitive at first. There are, however, two competing effects that negate each other so that the computed lifetime at $\sigma_{ff}^{0.5}$ is unchanged. These two competing effects are:

1. The overstressed length on an unbroken fiber near a fiber fracture location is reduced by a given factor at all times when compared to the control case. By itself this would tend to increase lifetimes.
2. Decreasing the overstressed length results in an increase in quasi-static strength, and hence, the far-field fiber stress level at which the simulation is performed i.e. $\sigma_{ff}^{0.5}$. By itself this would tend to decrease lifetime.

6 SUMMARY AND CONCLUSIONS

This paper develops a micromechanical technique for predicting the lifetime of unidirectional polymer composites loaded under tensile stress-rupture conditions. It is assumed that stress rupture in unidirectional composite materials occurs as a result of viscoelastic deformation in the matrix. The time-dependent response of the matrix causes an increase in the overstressed length on unbroken fibers near a cluster of fiber fractures. This increases the probability of failure of the unbroken fibers, and consequently the probability of failure of the composite material as a whole. The formulation presented in this work assumes linearly viscoelastic matrix behavior.

The first step in this effort is to develop a general framework for micromechanical stress redistribution due to an arbitrary sequence of fiber fractures. An approximate technique using Boltzmann superposition of time-dependent influence functions is developed. Two different sets

of influence-functions are calculated based on different shear-lag load-sharing assumptions. The first set of influence functions assume that the load of a broken fiber is redistributed only onto the nearest neighbors. This form of load sharing is termed Nearest Neighbor Load Sharing (NNLS) and it is developed because model composite experiments and finite element analysis of micromechanical load redistribution show that NNLS is applicable under quasi-static conditions (Bandorawalla *et. al.*, 2002b). The second set of time-dependent influence functions are developed by extending the traditional quasi-static analysis of Hedgepeth and Van Dyke (1967). A favorable comparison is made between the time-dependent load sharing analysis and measurements of the strain redistribution in model composites.

The load sharing framework is incorporated into a Monte Carlo simulation to predict the stress rupture lifetime of unidirectional composite materials. An encouraging comparison is made between predicted and measured lifetimes of a $[90/0_3]_s$ APC-2 composite laminate at 125°C and 140°C. Long-term time and temperature dependent viscoelastic properties of the matrix material are easily obtained by applying time-temperature superposition principles to short-term creep or relaxation data measured in a dynamic mechanical analyzer at several temperatures. This information is supplied to the simulation to predict long-term rupture lifetimes at any temperature. In this manner the simulations help understand and predict the role of temperature in accelerated measurement of stress rupture lifetimes. The extreme variability in rupture lifetimes makes it very important for predictive techniques to be able to assess composite reliability for a desired lifetime at a given stress level and temperature. The Monte Carlo simulation approach is particularly well suited to determine reliability under stress rupture conditions.

Measuring the stress-rupture lifetime of purely unidirectional composites is challenging because initial damage occurs in the gripped section of the specimen. The rupture lifetime of a unidirectional specimen is very sensitive to the number and location of the initial fiber fractures. Large initial damage in the gripped section necessarily leads to ultimate material failure in the gripped section. This paper puts forward recommendations to alleviate this problem by testing specimens with a $[90/0_n]_s$ layup. The surface 90° plies protect the 0° layers from damage in the

grip section while at the same time carrying a negligible fraction of the total load. Consistent gage section failures are observed when testing the $[90/0_3]_s$ APC-2 composite specimens.

In order to understand the reasons for large variability in computed rupture lifetimes a parametric study is performed by varying some of the input quantities to the model. It is shown that decreasing the variability in fiber strengths produces longer and more variable lifetimes. Unexpectedly, the rupture lifetime distribution is unchanged by altering the perturbed axial length due to a fiber fracture. This latter study is performed by changing a combination of geometric and material parameters such that the perturbed length is halved at all times. The lifetimes computed at a stress level that yields a 50% probability of instantaneous failure are unaffected.

The strength-life equal rank assumption is an intuitive argument that has no experimental basis, and it is very often used to simplify modeling efforts for life prediction of composite materials. A major conclusion of this work is to show that the strength-life equal rank assumption is not valid for longitudinally loaded unidirectional polymer composites, since an entirely different progression of fiber fractures leads to eventual composite failure when the far-field stress is continually increased (as with measuring fast-fracture strength) and when it is held constant (as with measuring stress-rupture lifetime).

Acknowledgements – The authors appreciate Professor K. L. Reifsnider's recommendations for improvement of this work. This work was supported by the Army Research Office (ARO Proposal No. 42451-EG).

REFERENCES

Bandorawalla T., McCord III, M. H., Case, S. W., 2002a. Micromechanical load redistribution in unidirectional polymer composites. Part I: Experiments. Composites science and technology.

Bandorawalla T., Russell B. E., Case, S. W., 2002b. Micromechanical load redistribution in unidirectional polymer composites. Part II: Modeling. Composites science and technology.

Beyerlein, I. J., Phoenix, S. L., Raj, R., 1998. Time evolution of stress redistribution around multiple fiber breaks in a composite with viscous and viscoelastic matrices. International Journal of Solids and Structures 35 (24), 3177-3211.

Du, Z. Z., McMeeking, R M., 1995. Creep models for metal matrix composites with long brittle fibers. Journal of the Mechanics and Physics of Solids 43 (5), 701-726.

Hedgepeth, J. M., 1961. Stress concentrations in filamentary structures. NASA TN D-882, Langley Research Center.

Hedgepeth, J. M., Van Dyke, P., 1967. Local stress concentrations in imperfect filamentary composite materials. Journal of Composite Materials 1, 294-309.

Ibnabdeljalil, M., Phoenix, S. L., 1995. Creep rupture of brittle matrix composites reinforced with time dependent fibers: scalings and Monte Carlo simulations. Journal of the Mechanics and Physics of Solids 43 (6), 897-931.

Iyengar, N., Curtin, W. A., 1997a. Time-dependent failure in fiber-reinforced composites by fiber degradation. Acta Materialia 45 (4), 1489-1502.

Iyengar, N., Curtin, W. A., 1997b. Time-dependent failure in fiber-reinforced composites by matrix and interface shear creep. Acta Materialia 45 (8), 3419-3429.

Lagoudas, D. C., Hui, C., Phoenix, S. L., 1989. Time evolution of overstress profiles near broken fibers in a composite with a viscoelastic matrix. International Journal of Solids and Structures 25 (1), 45-66.

Landis, C. M., Beyerlein, I. J., McMeeking, R. M., 2000. Micromechanical simulation of the failure of fiber reinforced composites. Journal of the Mechanics and Physics of Solids 48, 621-648.

Lifshitz, J. M., 1971. MED Report No. 33. Department of Materials Engineering, Technion, Israel.

Lifshitz, J. M., Rotem, A., 1970. Time-dependent longitudinal strength of unidirectional fibrous composites. Fibre Science and Technology 3, 1-20.

Otani, H., Phoenix, S. L., Petrina, P., 1991. Matrix effects on lifetime statistics for carbon fiber-epoxy microcomposites in creep rupture. Journal of Materials Science 26, 1955-1970.

Phoenix, S. L., Schwartz, P., Robinson IV, H. H., 1988. Statistics for the strength and lifetime in creep-rupture of model carbon/epoxy composites. Composites Science and Technology 32, 81-120.

Schapery, R. A., 1967. Stress analysis of viscoelastic composite materials. Journal of Composite Materials 1, 228-267.

Wimolkiatisak, A. S., Bell, J. P., 1989. Interfacial shear strength and failure modes of interphase-modified graphite-epoxy composites. Polymer Composites 10 (3), 162-172.

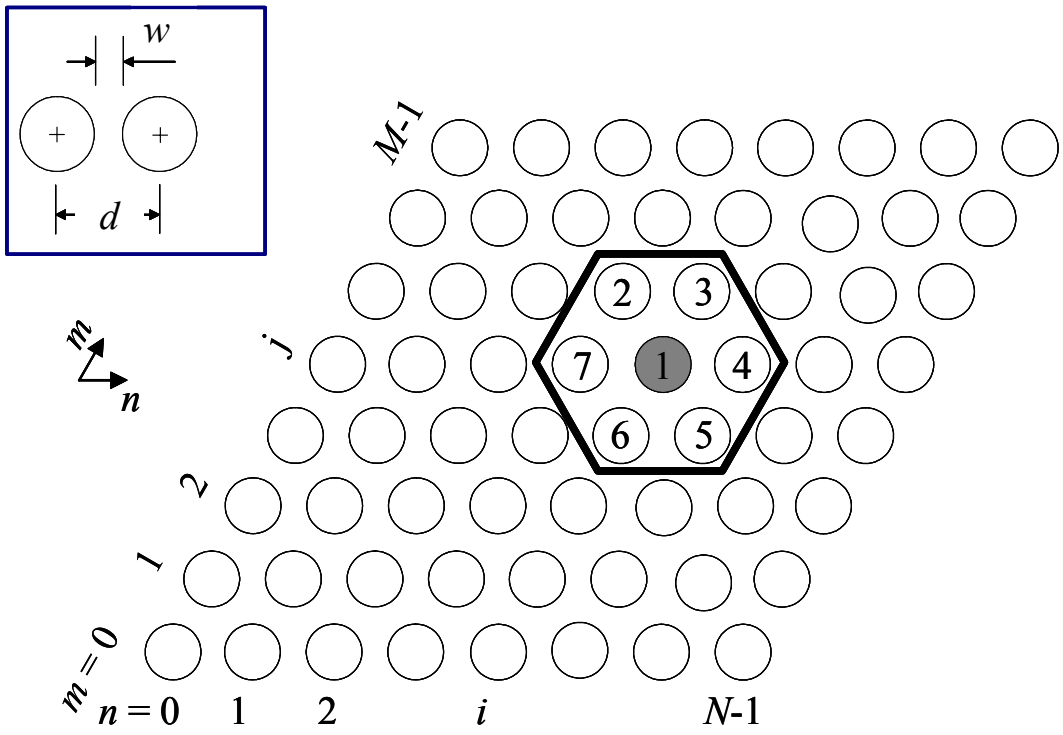

Figure 1. Hexagonally packed array of fibers with fiber numbering scheme

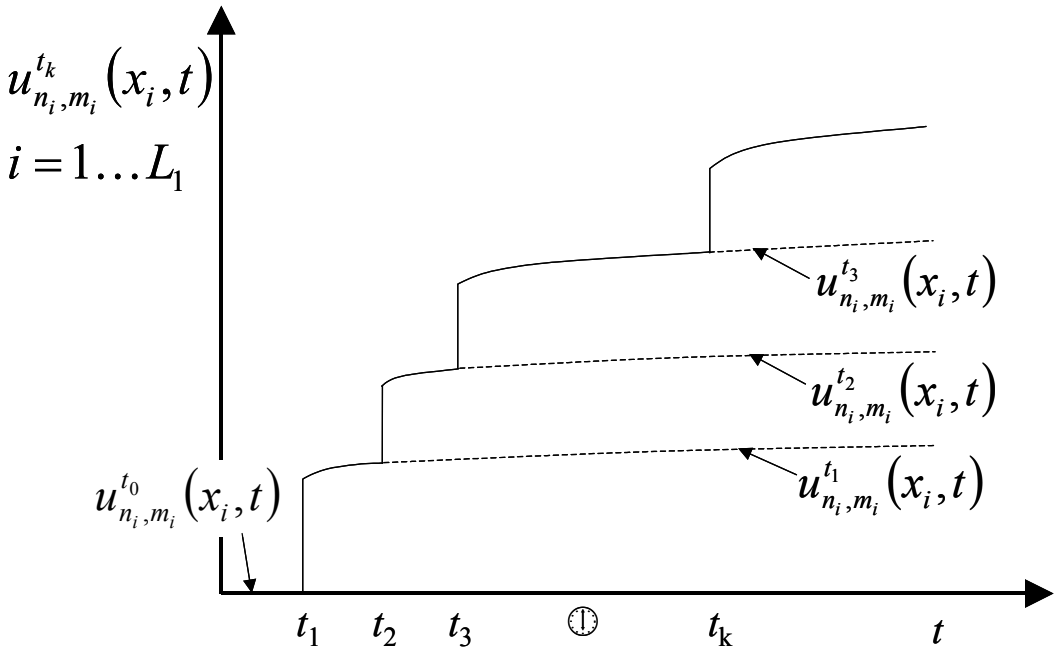

Figure 2. Break opening-displacements for breaks 1…L_1 due to first L_k fractures

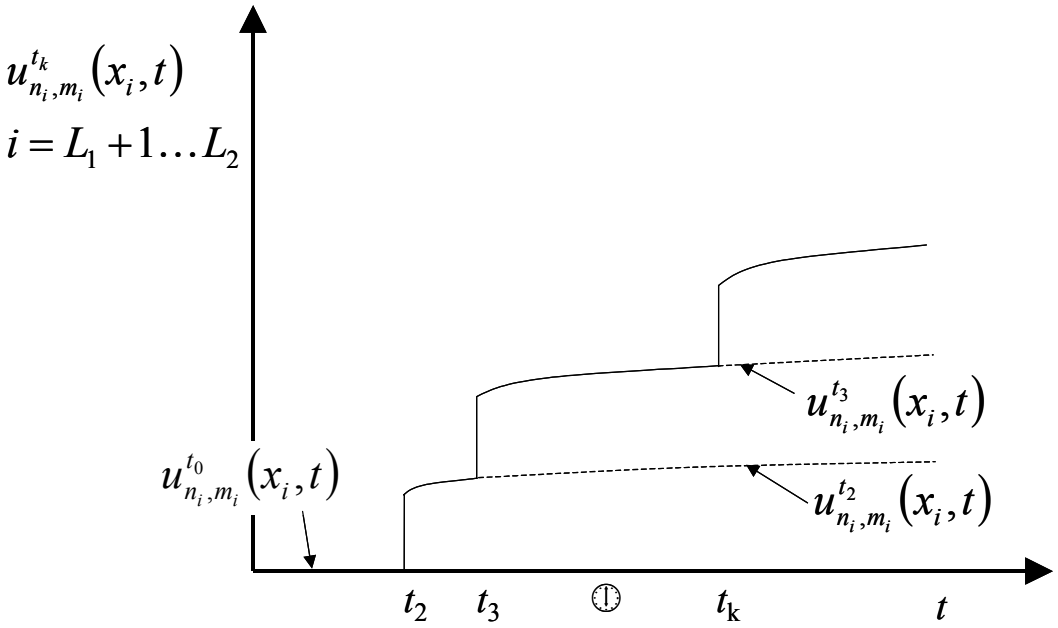

Figure 3. Break opening-displacements for breaks L_1+1…L_2 due to first L_k fractures

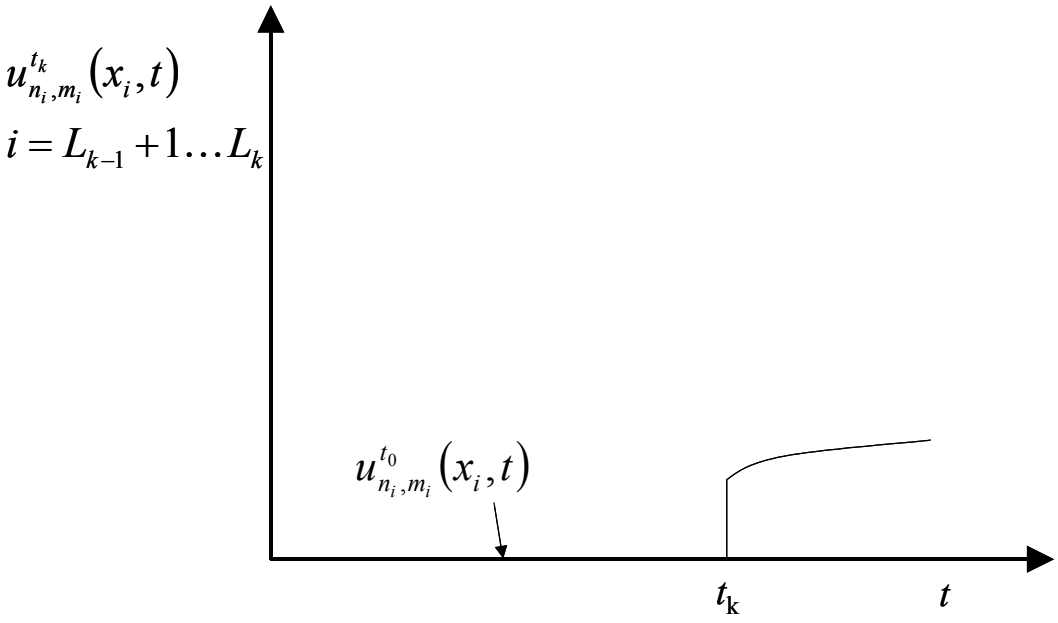

Figure 4. Break opening-displacements for breaks L_{k-1}+1…L_k due to first L_k fractures

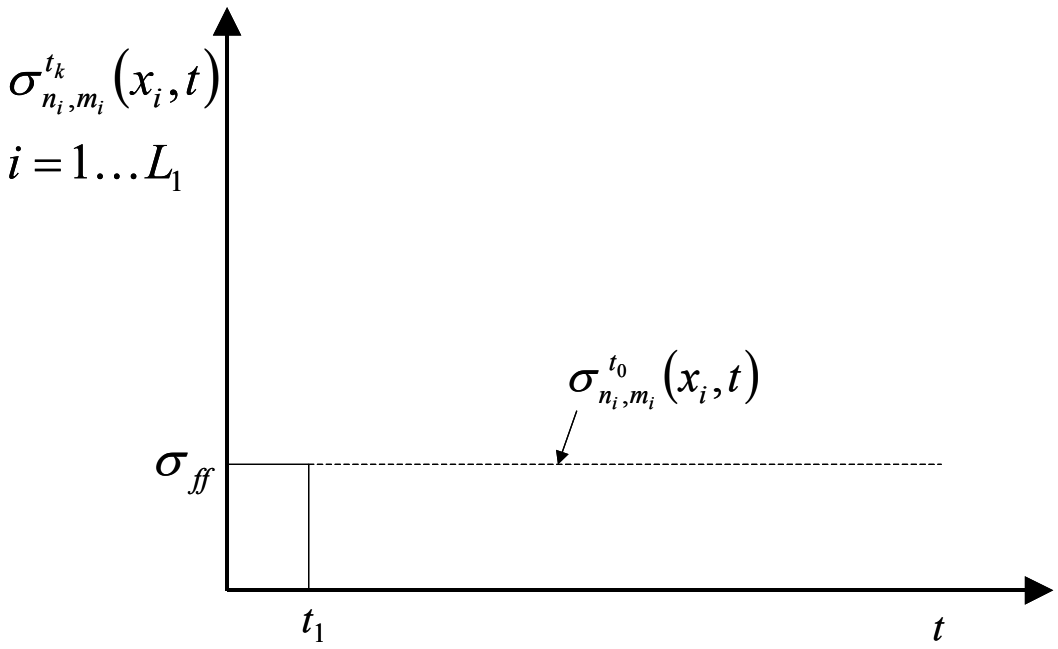

Figure 5. Fiber stresses at breaks 1…L_1 due to first L_k fractures

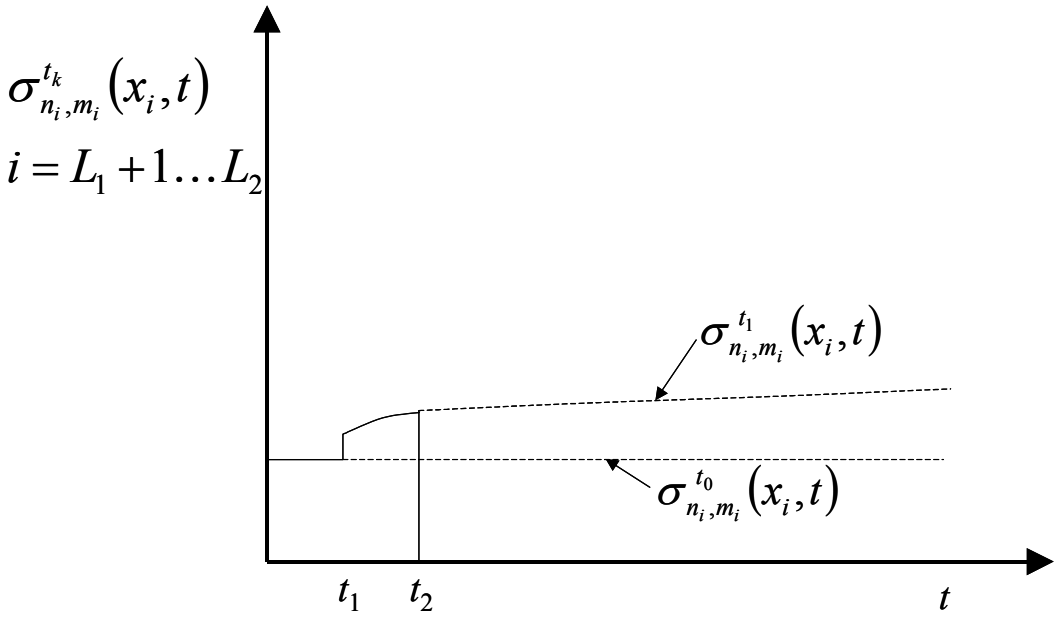

Figure 6. Fiber stresses at breaks L_1+1…L_2 due to first L_k fractures

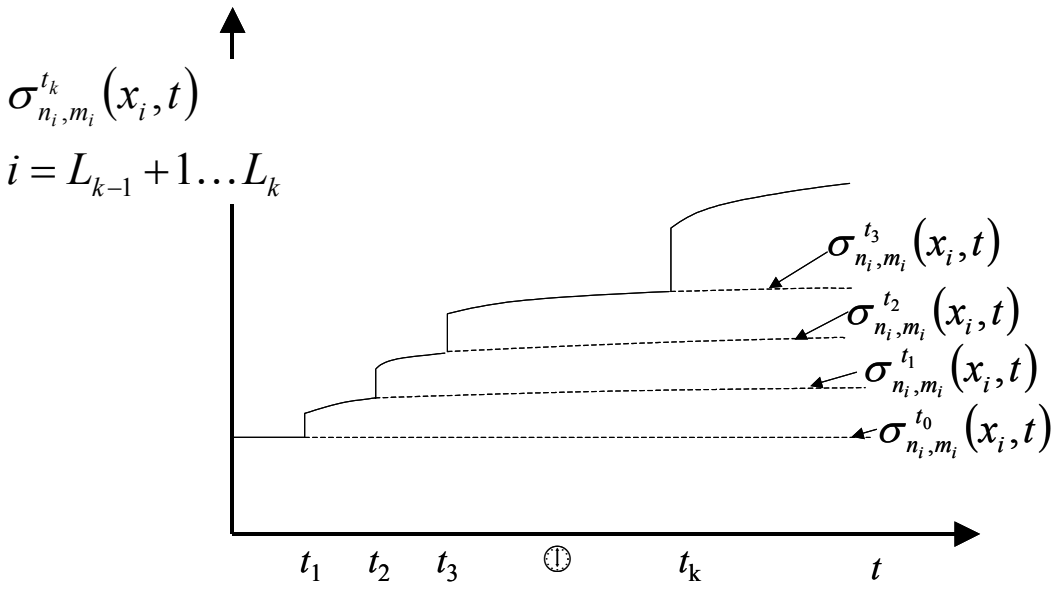

Figure 7. Fiber stresses at breaks $L_{k-1}+1 \ldots L_k$ due to first L_k fractures

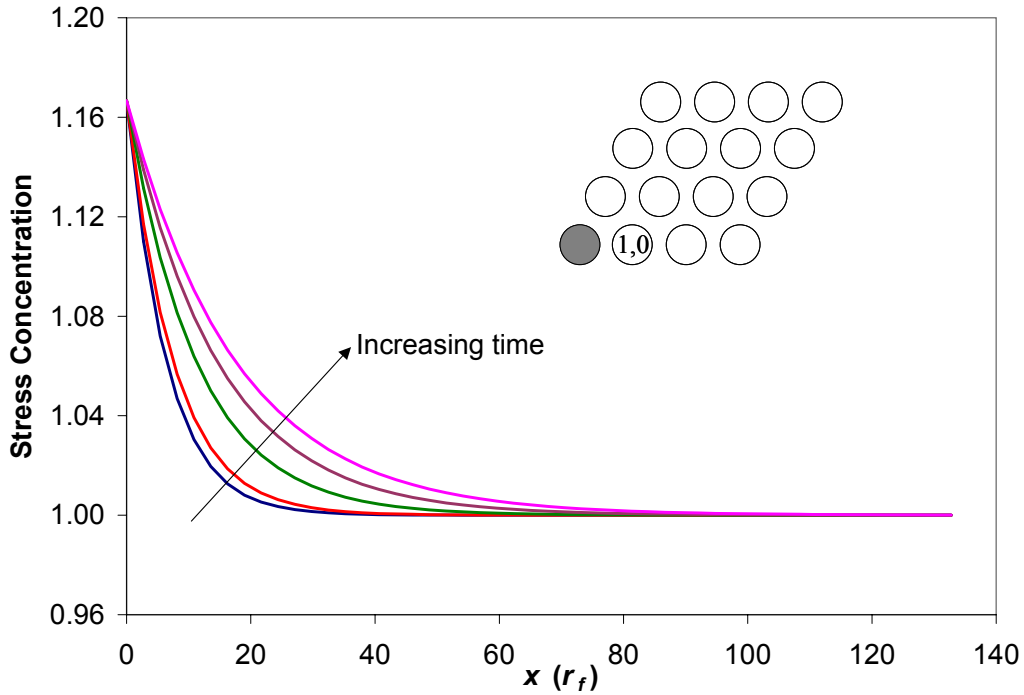

Figure 8. Stress in fiber (1,0) due to isolated break in shaded fiber at $x = 0$ computed with NNLS

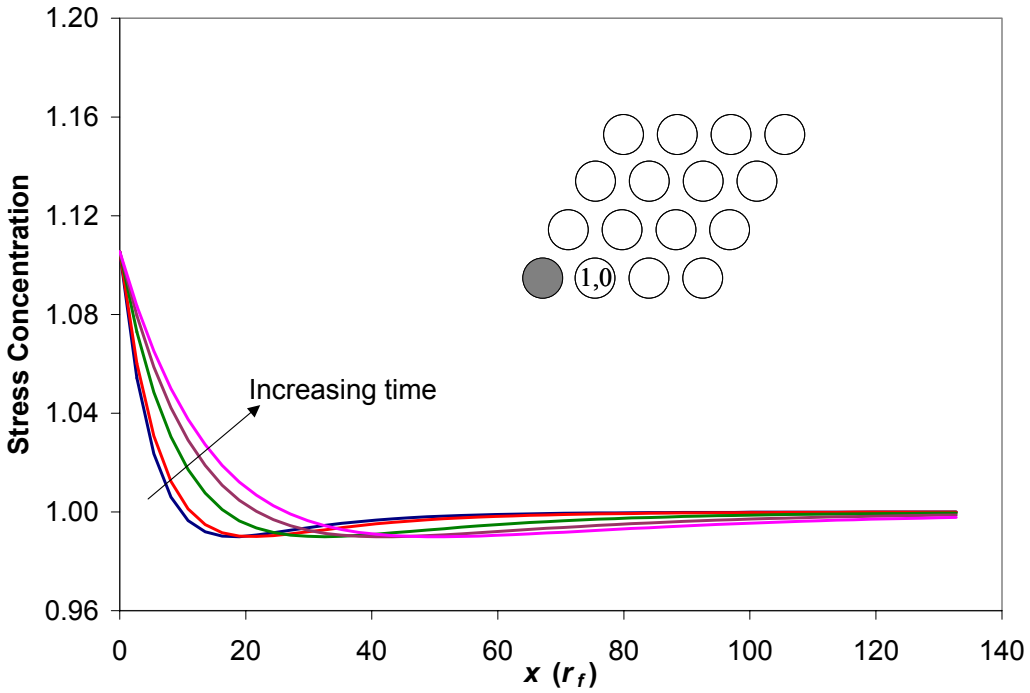

Figure 9. Stress in fiber (1,0) due to isolated break in shaded fiber at $x = 0$ computed with HVDLS

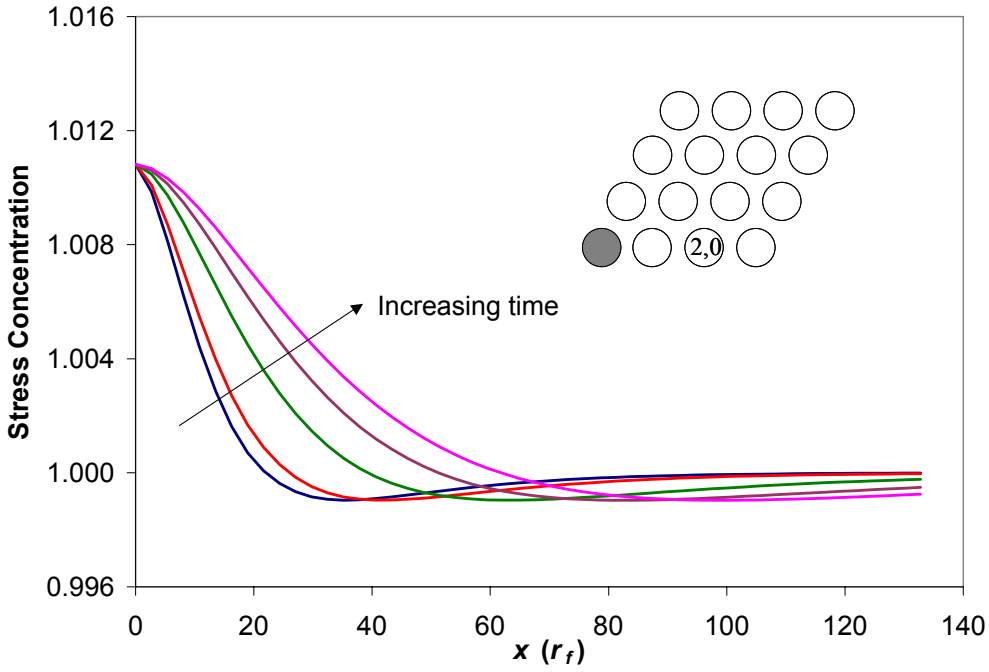

Figure 10. Stress in fiber (2,0) due to isolated break in shaded fiber at $x = 0$ computed with HVDLS

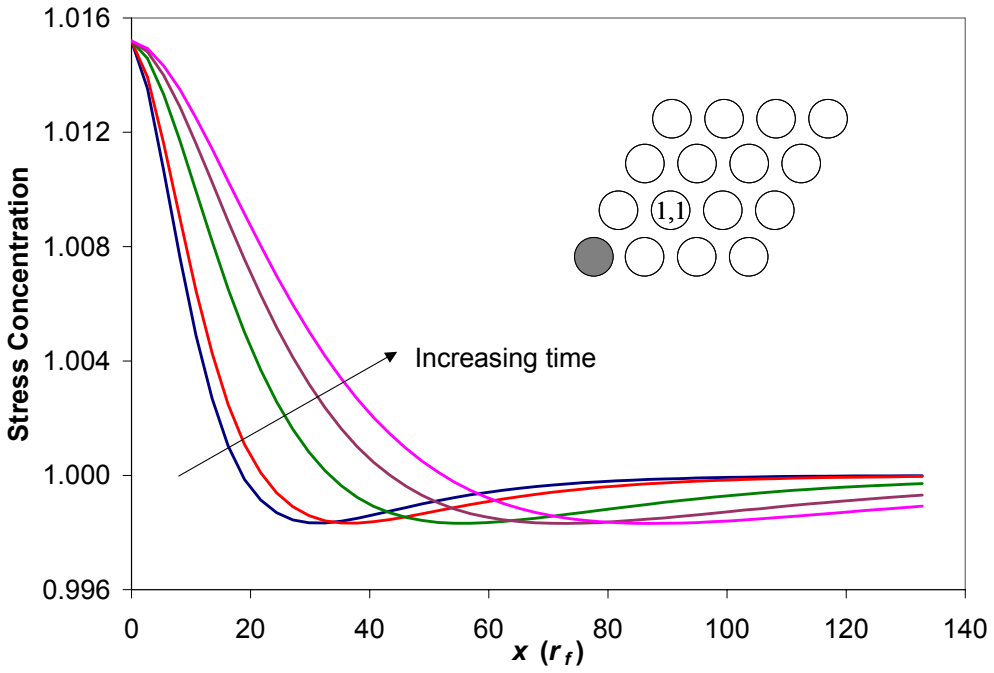

Figure 11. Stress in fiber (1,1) due to isolated break in shaded fiber at $x = 0$ computed with HVDLS

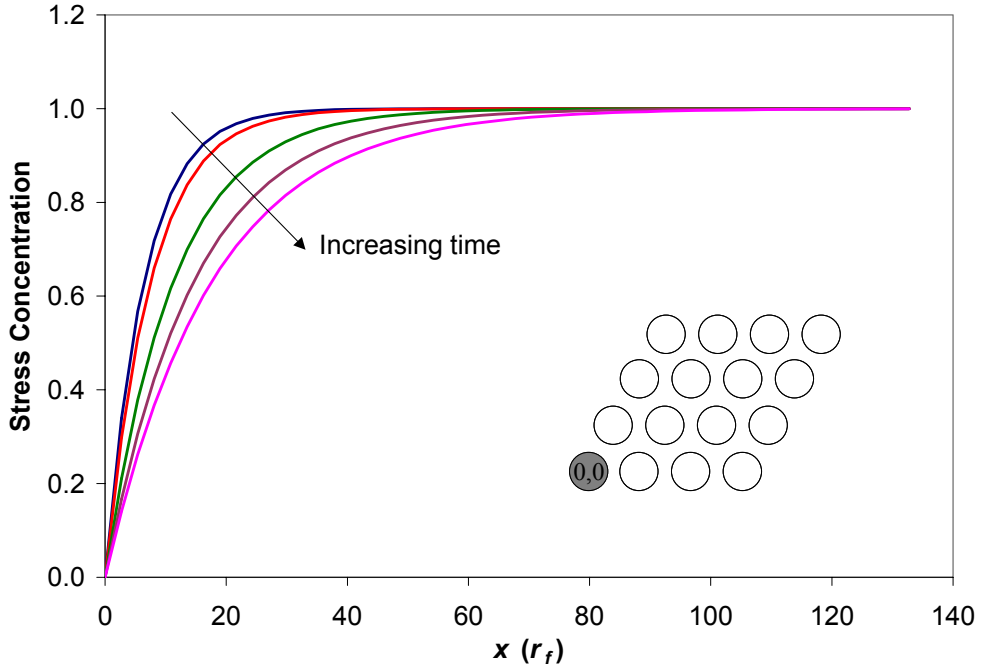

Figure 12. Stress in broken fiber (0,0) due to isolated break at $x = 0$ computed with NNLS

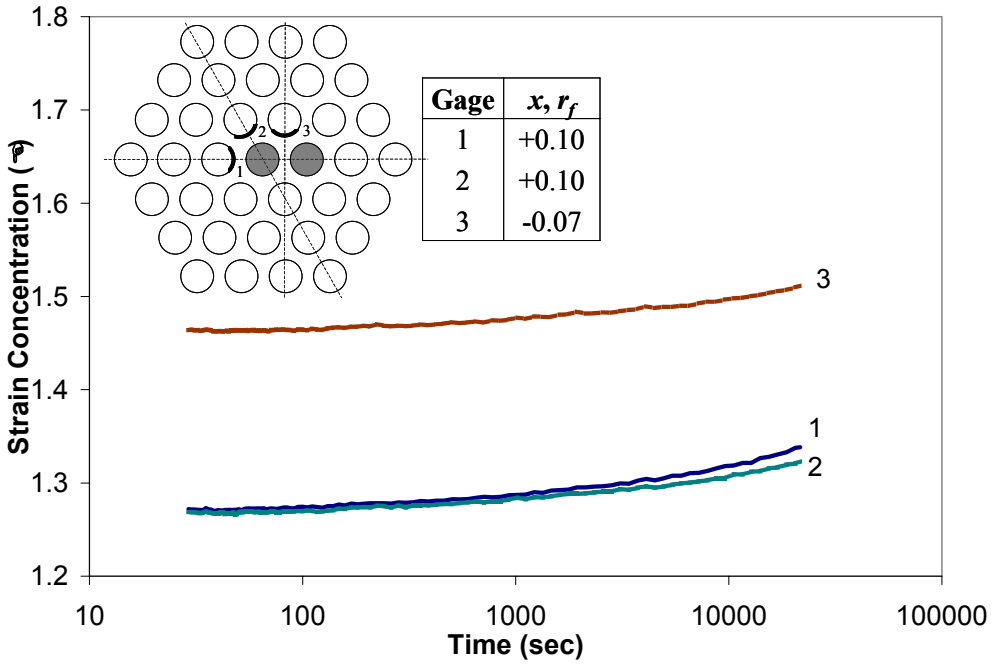

Figure 13. Model composite measurements of strain concentrations due to a two adjacent coplanar fiber fractures

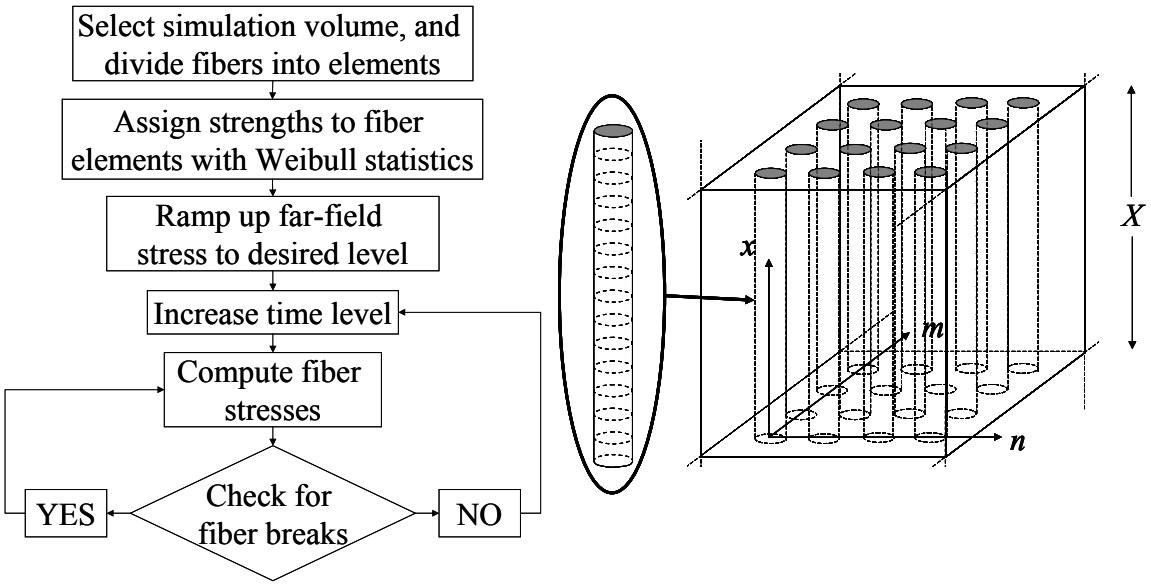

Figure 14. Flowchart of Monte Carlo simulation for stress rupture lifetime with representative volume element (RVE)

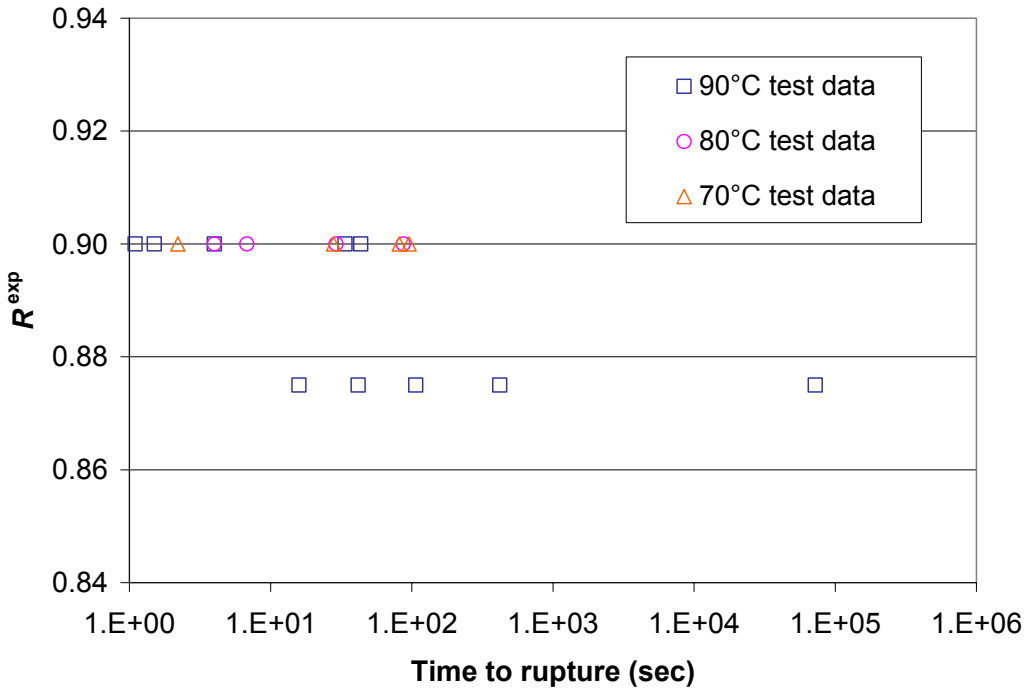

Figure 15. Stress rupture lifetimes of Grafil carbon fiber/PPS unidirectional composite

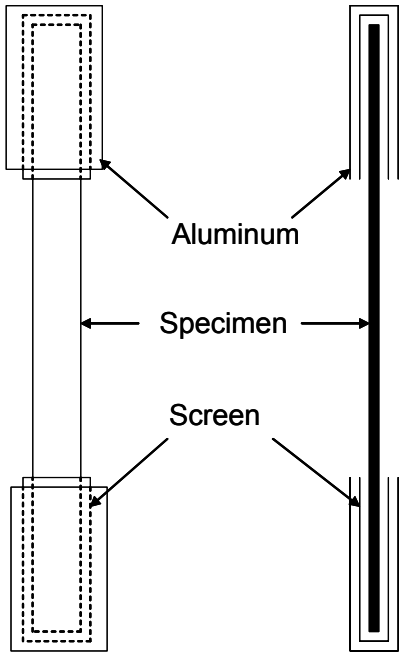

Figure 16. Tabbing of specimens for tensile strength and stress rupture testing

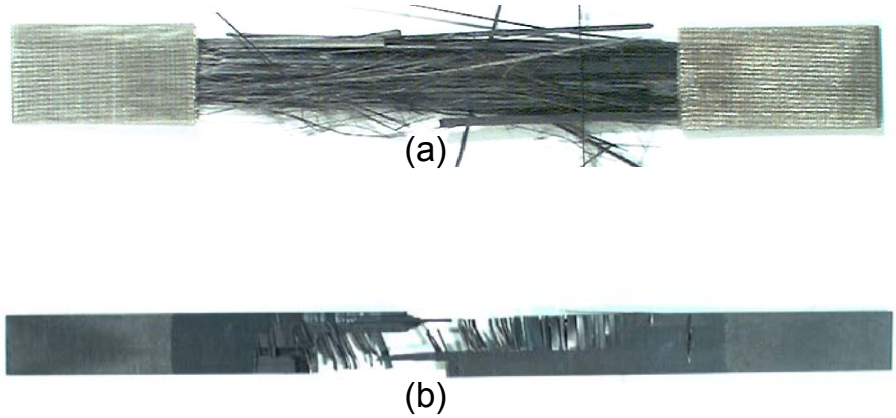

Figure 17. Failed specimens. (a) Grafil carbon fiber/PPS unidirectional composite (b) APC-2 $[90/0_3]_s$ laminate

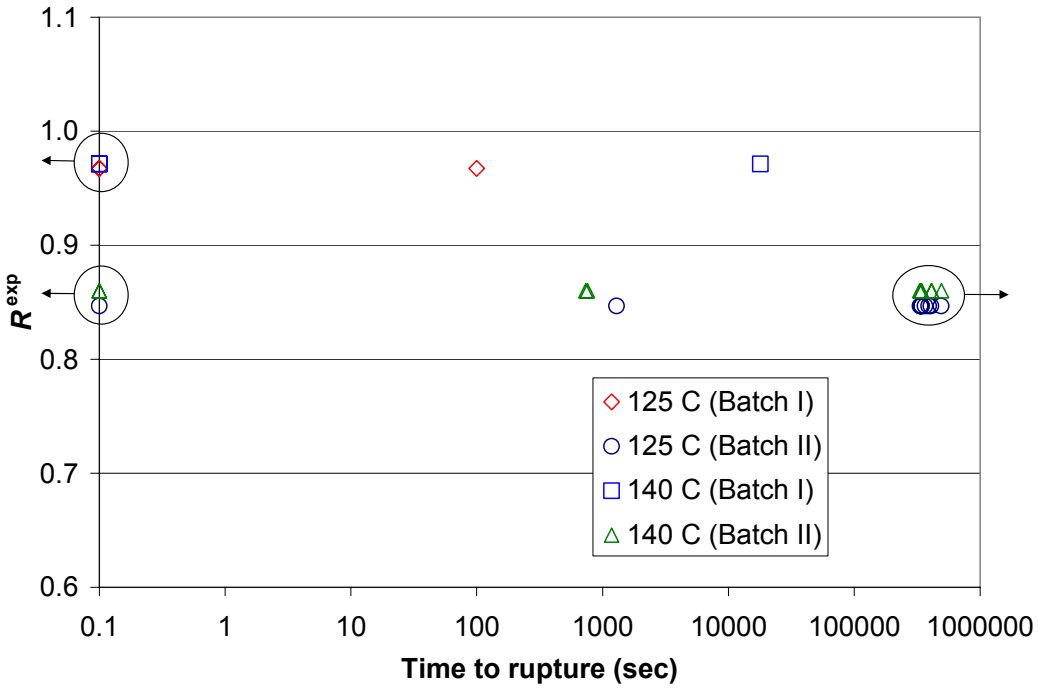

Figure 18. Stress rupture lifetime of APC-2 $[90/0_3]_s$ specimens

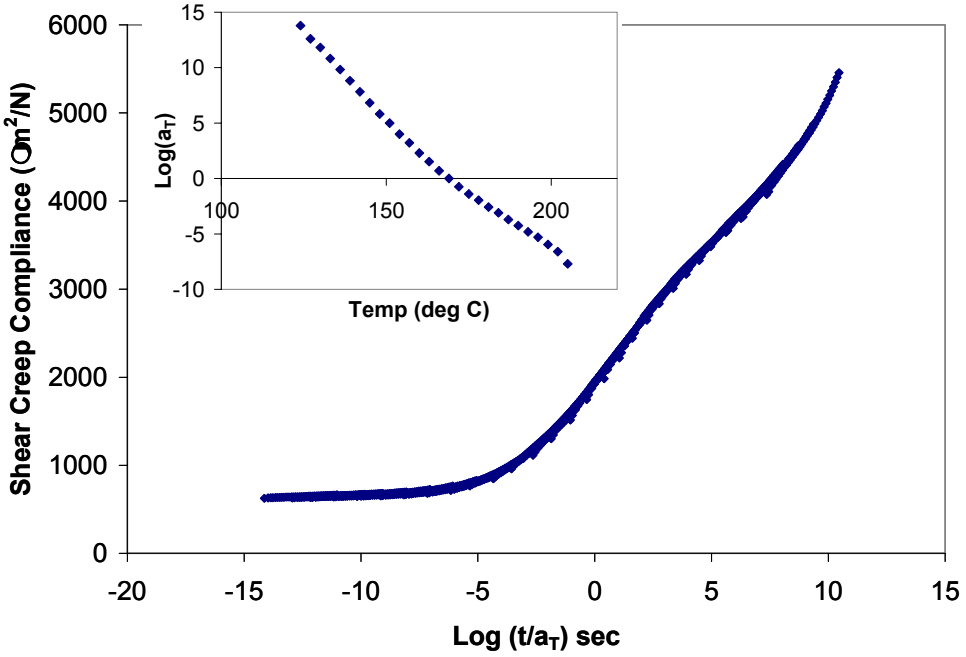

Figure 19. Master curve and shift factors for shear creep compliance of PEEK

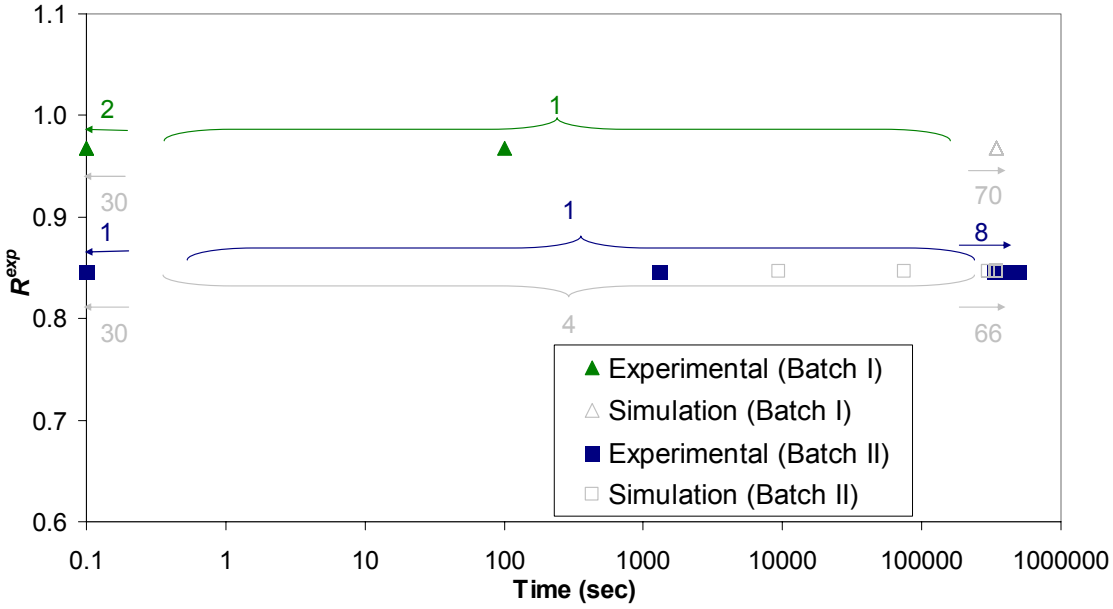

Figure 20. Rupture lifetime predictions for APC-2 composite at 125°C (NNLS)

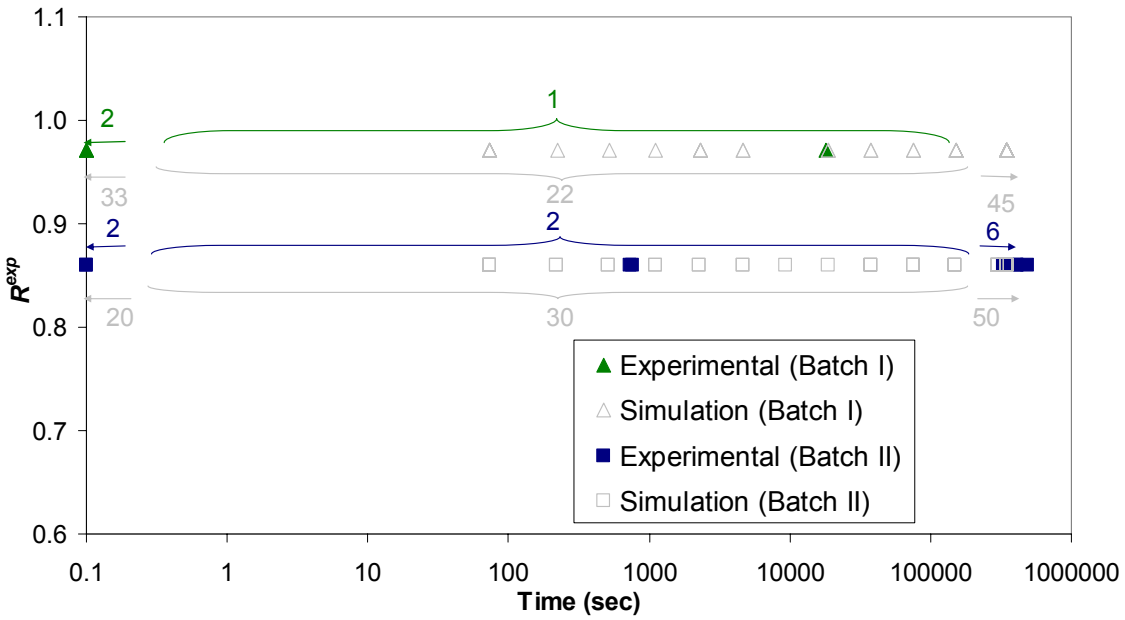

Figure 21. Rupture lifetime predictions for APC-2 composite at 140°C (NNLS)

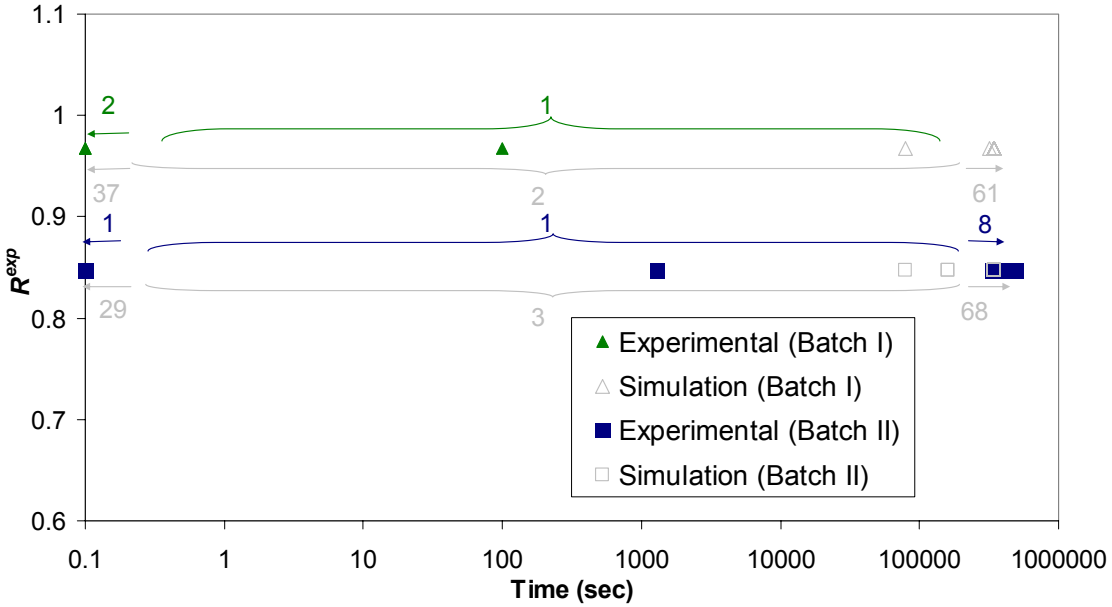

Figure 22. Rupture lifetime predictions for APC-2 composite at 125°C (HVDLS)

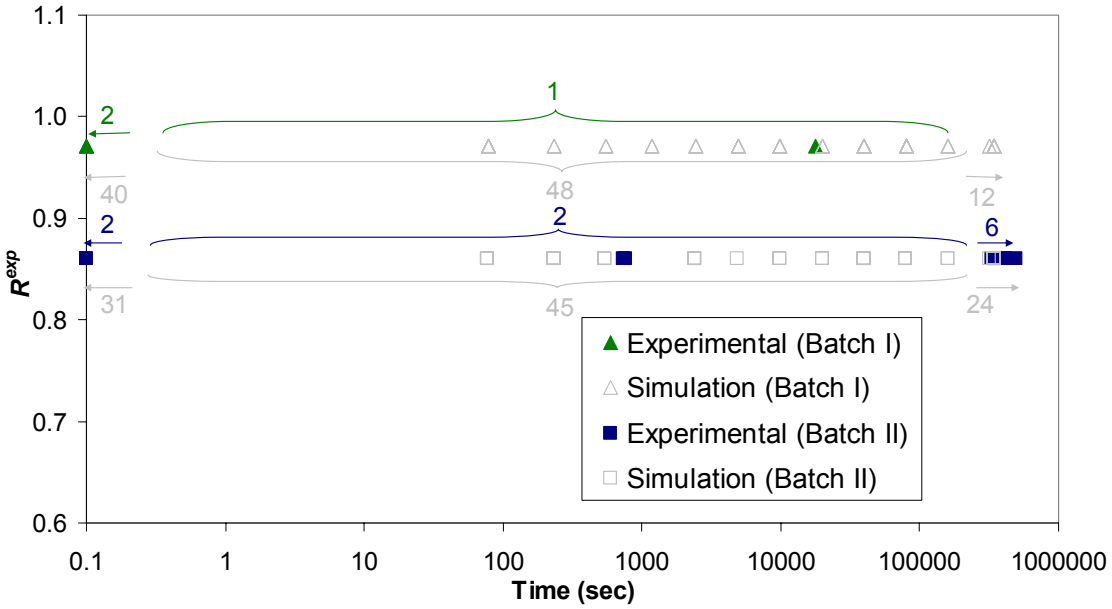

Figure 23. Rupture lifetime predictions for APC-2 composite at 140°C (HVDLS)

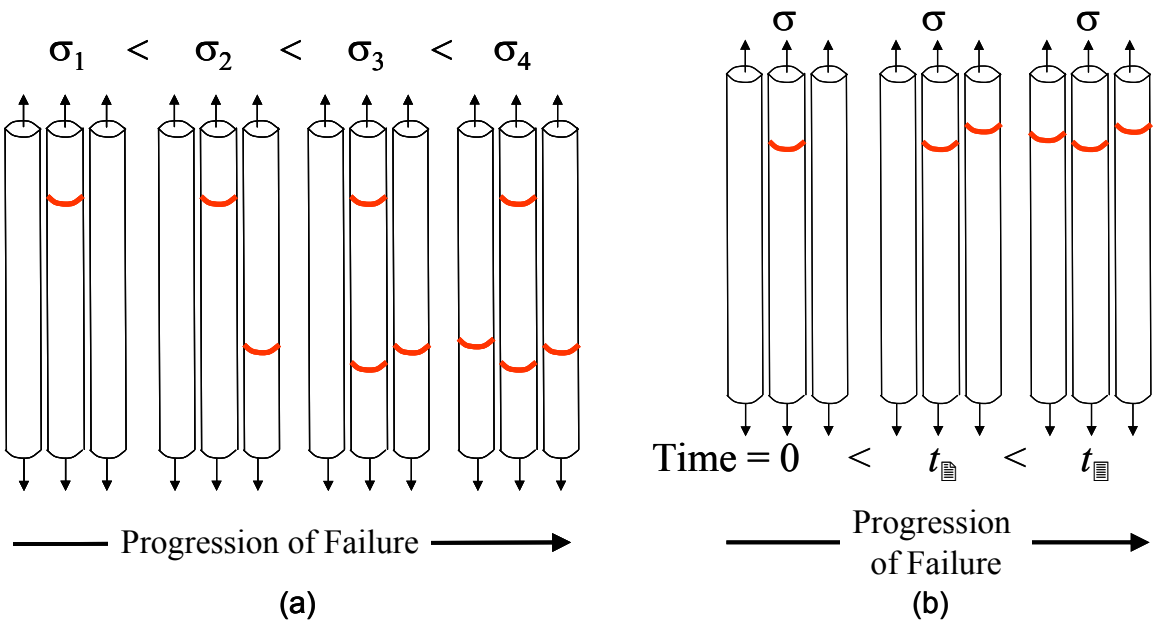

Figure 24. Failure behavior of unidirectional polymer composites. (a) Quasi-static failure (b) Stress-rupture failure

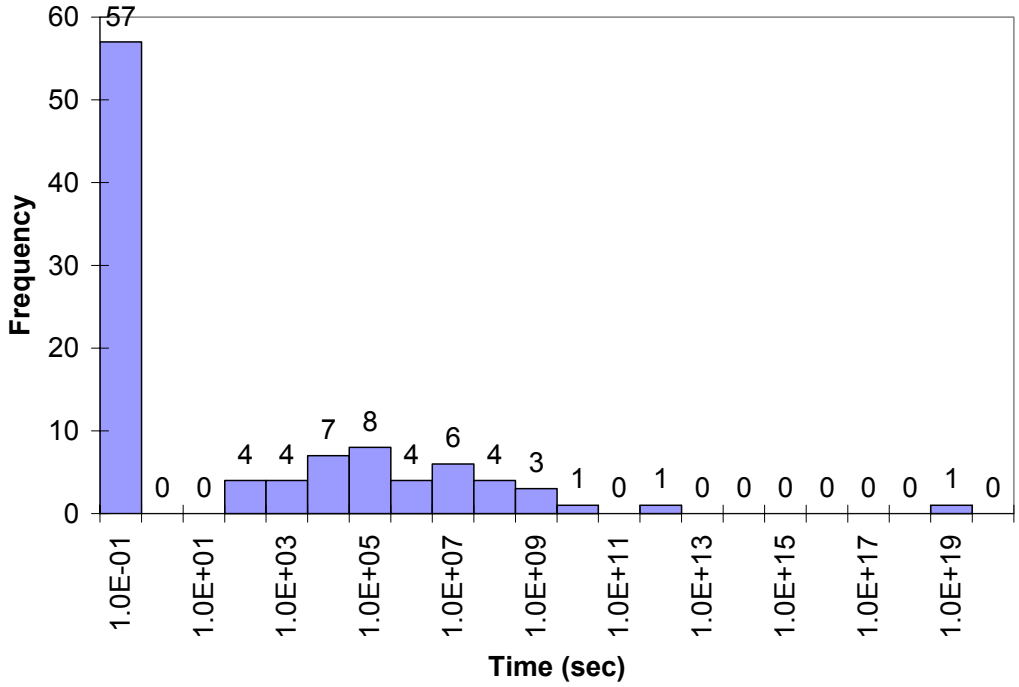

Figure 25. Lifetime distribution for control case

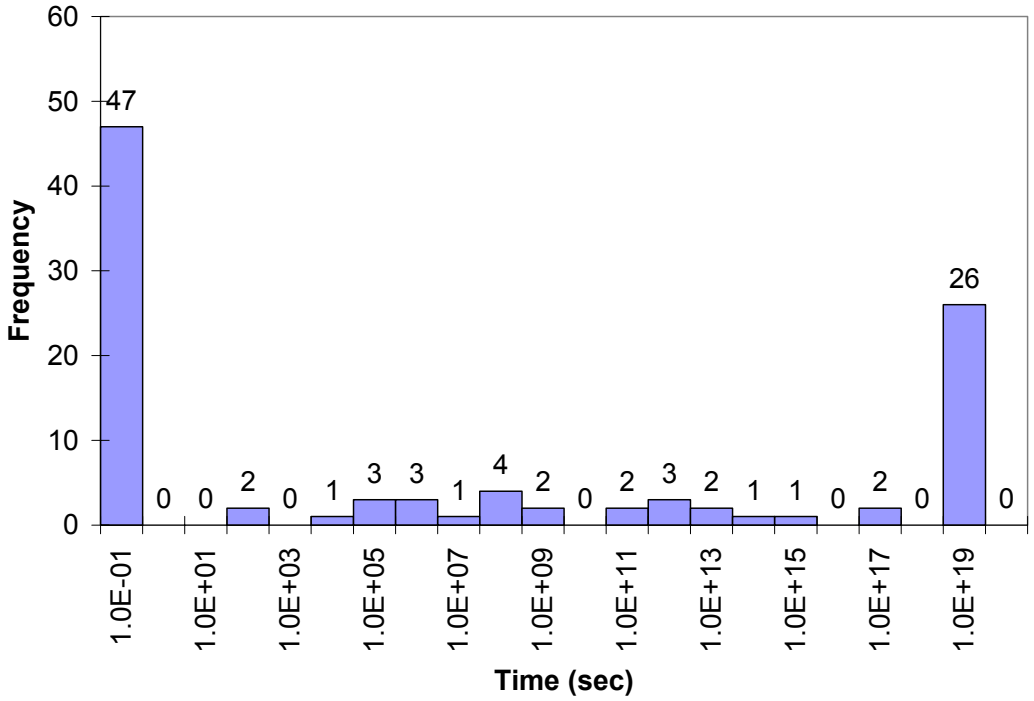

Figure 26. Lifetime distribution with narrower fiber strength distribution

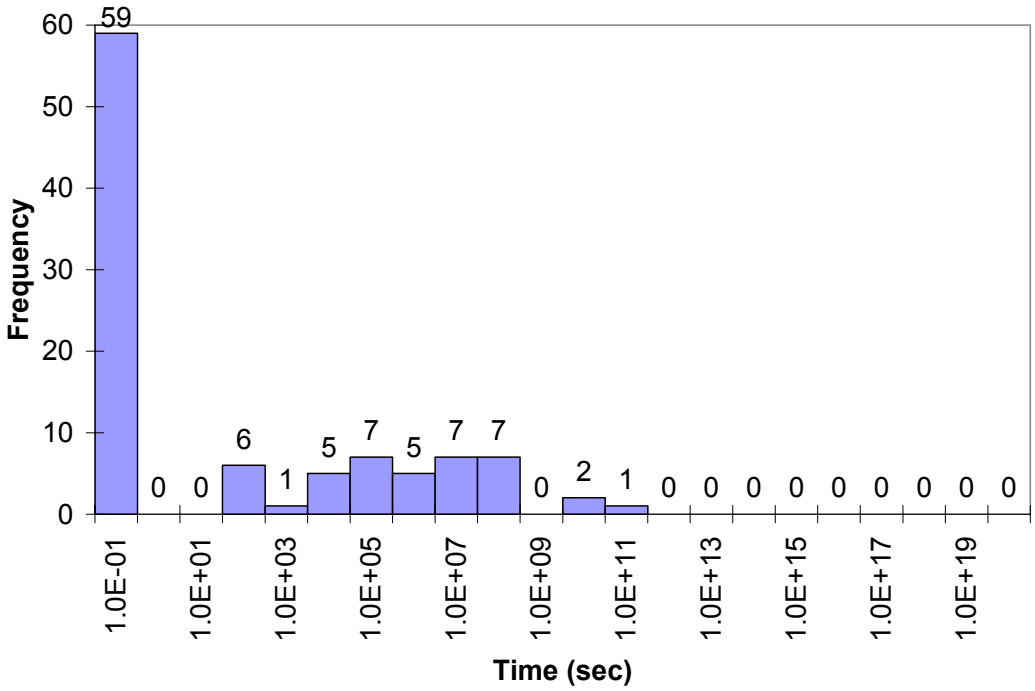

Figure 27. Lifetime distribution with shorter perturbed axial length along a broken or neighboring fiber due to a fiber fracture

Table 1. Quasi-static strength of APC-2 $[90/0_3]_s$ (strengths reported at 76 mm gage length)

	BATCH I		BATCH II	
	$\tilde{\sigma}_o^{\exp}$ **(GPa)**	$\tilde{m}^{\exp}$	$\tilde{\sigma}_o^{\exp}$ **(GPa)**	$\tilde{m}^{\exp}$
125°C	1.56	24.7	1.78	6.6
140°C	1.42	32.3	1.69	9.0

Table 2. Quasi-static strength predictions of unidirectional APC-2 V_f = 54% obtained by applying two different load-sharing techniques (strengths reported at X = 0.47 mm)

	$\widetilde{\sigma}_o^{\text{sim}}$	$\widetilde{m}^{\text{sim}}$
NNLS	2.60	47.5
HVDLS	2.72	80.1